

Single-particle and collective excitations in quantum wires comprised of vertically stacked quantum dots: Finite magnetic field

Manvir S. Kushwaha¹

Department of Physics and Astronomy, Rice University, P.O. Box 1892, Houston, TX 77251, USA

¹ *Corresponding Author: manvir@rice.edu*

(Dated: February 13, 2022)

Abstract

A theoretical investigation has been made of the magnetoplasmon excitations in a quasi-one-dimensional electron system comprised of vertically stacked, self-assembled InAs/GaAs quantum dots. The smaller length scales involved in the experiments impel us to consider a perfectly periodic system of two-dimensionally confined InAs quantum dot layers separated by GaAs spacers. Subsequent system is subjected to a two-dimensional confining (harmonic) potential in the x-y plane and an applied magnetic field (B) in the symmetric gauge. This scheme defines virtually a system of quantum wire comprised of vertically stacked quantum dots (VSQD). We derive and discuss the Dyson equation, the generalized (nonlocal and dynamic) dielectric function, and the inverse dielectric function for investigating the single-particle and collective (magnetoplasmon) excitations within the framework of (full) random-phase approximation (RPA). As an application, we study the influence of the confinement potential and the magnetic field on the component eigenfunctions, the density of states (DOS), the Fermi energy, the collective excitations, and the inverse dielectric functions. How the B-dependence of DOS validate the VSQD mimicking the realistic quantum wires, the Fermi energy oscillates as a function of the Bloch vector, the intersubband single-particle continuum bifurcates at the origin, a collective excitation emerges and propagates within the gap of the split single-particle continuum, and the alteration in the well- and barrier-widths allows to customize the excitation spectrum in the desired energy range are some of the remarkable features of this investigation. These findings demonstrate, for the very first time, the significance of investigating the system of VSQD subjected to a quantizing magnetic field. Given the edge over the planar quantum dots and the foreseen applications in the single-electron devices and quantum computation, investigating the system of VSQD is deemed vital. The results suggest exploiting magnetoplasmon qubits to be a potential option for implementing the solemn idea of quantum state transfer in devising quantum gates for the quantum computation and quantum communication networks.

PACS numbers: 73.21.-b, 73.63.-b, 75.47.-m, 78.20.Ls

I. INTRODUCTION

A closer look at the literature of condensed-matter physics of the past three decades reveals the impact, the legacy, and the ongoing influence of the man-made, quasi- n -dimensional, semiconducting heterostructures – n ($= 2, 1$, or 0) being the degree of freedom – on the current (and the near future) science and technology. Thanks to the wishful advancements in the nanofabrication technology and the electron lithography, these quantum structures have made possible the emergence of much of the exotic – fundamental and applied – physics transpired during this period. The continued interest in the physics and fabrication of such tailor-made nanostructures is triggered by the world-wide drive to develop exciting high-speed, low-threshold devices that are small enough, sharp enough, or uniform enough to behave the way theory says they should. Fabricated mostly from III-V compounds and fashionably becoming known as the quantum wells (with $n = 2$), quantum wires (with $n = 1$), and quantum dots (with $n = 0$), these nanostructures represent the systems in which the charge carriers exposed to external electric and/or magnetic fields can (and do) manifest unusual quantal effects that strongly alter their behavior characteristics [1].

It is beyond dispute that the discovery of quantum Hall effects – both integer and fractional – had spurred the research interest in semiconducting systems of lower dimensions, which keeps electrifying a vast majority of condensed matter physicists [1]. The emergence of graphene in 2004 and its device potential quickly stimulated researchers to inquire into other materials of the same descent, which include germanene and silicene. The optimism in the research on the ...enes has also prompted several research groups to explore layered materials such as nitrides, oxides, selenides, sulfides, and tellurides, which have gradually joined the long list of largely exploited arsenides, antimonides, and phosphides. Consequently, the making of nanostructures like nanoribbons, nanowires, nanoballs, nanorods, nanogrids, nanopillars, nanosnakes, nanoonions, ...etc. keeps researchers captivated by the miniaturization. However, nothing compares to the total confinement of quantum dots, which have many features in common with the real atoms. Nevertheless, the pivotal difference is mesmerizing: numerous electronic, optical, and transport properties in quantum dots are tunable – unlike in the real atoms. The tunability allows the wishful control and manipulation of the charge carriers in the system. This makes the quantum dots, especially the self-assembled quantum dots, the real gems for devising nanodevices, which forge the foundation of future nanoscience and nanotechnology.

Smaller length scales (of a few nanometers) involved in the experimental setup prompt us to consider a perfectly periodic system of two-dimensionally confined InAs quantum dot layers separated by GaAs spacers. Given the adequate lateral confinement and vertical coupling, the resultant system

can be made to mimic the quantum wires comprised of quantum dots. The readers are reminded of certain facts which motivate us to exploit the periodic system of VSQD for the device designing. These are: (i) Sakaki's meticulous diagnosis that led him to justify the designing of such heterostructures in which the optical phonon scattering can be essentially eliminated [2]; (ii) the methodical justification for the use of Fermi-liquid-like theories for describing the realistic quantum wires [3]; (iii) the strain due to lattice mismatch at the interfaces, which provides impetus for the growth of self-assembled quantum dots in the system [4, 5]; (iv) the wishful tunability of the coupling strength, which not merely paves the way to interesting applications in quantum computation and spintronics, it also allows exploring new fundamental physics of steering spins and controlling electron g factors [6]; and (v) the robust coupling strength along the growth axis rendering a quasi-one-dimensional (Q1D) system devised of quasi-zero-dimensional (Q0D) systems. Here item (v) fulfills the quest for *reversing the trend*, i.e., fabricating the systems of higher dimensions [1]: 0 to 1, 1 to 2, and 2 to 3.

Research interest in the system of VSQD fabricated out of InAs islands separated by GaAs spacers along the growth axis was triggered by early experiments in the mid-1990s [4-6]. The foreseen device potential of the VSQD system immediately prompted many research groups embarking on the wide-ranging investigations. Consequently, diverse experimental [7-56] and theoretical [57-76] works started dealing with electronic, optical, and transport phenomena, which persuaded authors to envision diverse solid-state devices. The early focus remained primarily on the quantum-dot molecules (QDM) made up of the pairs of VSQD separated by thin barriers. The reason was their significance in realizing the short-range quantum-state transfers. As a matter of fact, this concept proved to be consequential for the future quantum communication networks. In most cases, it is imperative to stack multiple VSQD in order to allow a larger flux of emitted or absorbed photons. Their aerial number density depends on the specific use, however.

Initial experimental as well as theoretical focus – based on the shape, size, and setup of the VSQD – had mainly been restricted to a single isolated qubit, whereas the real fuss in quantum computation calls for creating and controlling entanglement of multiple qubits. The basic notion in realizing the quantum gates, which are the salient units of quantum communication networks, rests in the consistent manipulation of exciton qubits. Interestingly, the role of an applied magnetic field relevant to the (nuclear or electron) polarization does not seem to be cherished enough in the VSQD. In spite of the exotic role played by the magnetoplasmon excitations in the electronic, optical, and transport phenomena in diverse quantum nanostructures [1], the literature is still devoid of any report on proposing novel magnetoplasmon qubits (MPQ), which offer a greater speed advantage over the ritual exciton qubits in the VSQD. This article tends to fill that void.

The rest of the article is organized as follows. In Sec. II, we present the methodological framework leading to the derivation of the nonlocal, dynamic, dielectric function (within the full random-phase approximation (RPA) [77]), which is further scrutinized to fully address the solution of the problem and the relevant physics. In Sec. III, we discuss several illustrative examples of, for instance, the density of states, the Fermi energy, Coulomb interaction, the single-particle and collective excitation spectrum, ...etc. There, we also examine the effects of an applied magnetic field and the influence of alteration in the well- and barrier-thicknesses on the excitation spectrum. In addition, we call attention to the importance of studying inverse dielectric function in connection with the quantum transport phenomena in the system [78]. Finally, in Sec. IV, we summarize our findings and highlight some interesting features worth adding to the problem.

II. THEORETICAL FRAMEWORK

A. Eigenfunctions and eigenenergies

We consider a periodic system of quasi-two-dimensional InAs islands of thickness a separated by GaAs spacer layers of thickness b . The InAs islands are constrained by a two-dimensional confining (harmonic) potential of the form of $V(x) = \frac{1}{2}m^*\omega_0^2(x^2 + y^2)$ in the x-y plane and subjected to an applied magnetic field (B) in the symmetric gauge specified by the vector potential $\mathbf{A} = \frac{1}{2}B(-y, x)$. This choice of the vector potential preserves the gauge invariance brought about by the so-called gauge transformation that requires the electromagnetic fields \mathbf{E} and \mathbf{B} to remain the same. We assume the growth axis to be under a robust confining potential, $V_c(z)$, yielding strong coupling between InAs layers. The small length scales and strong coupling make the final system of VSQD (see Fig. 1) mimic a realistic quantum wire with a well-defined *linear* charge density and hence legitimize the tight-binding approximation (TBA) [62]. The moderate tunneling (in the polarizability function) is accounted for with the energy dispersion being sinusoidal. The effective quantum wire is characterized by the single-particle [of charge $-e$, with $e > 0$] Hamiltonian

$$H = \frac{1}{2m^*} \left[\left(p_x + \frac{e}{c}A_x \right)^2 + \left(p_y + \frac{e}{c}A_y \right)^2 \right] + \frac{1}{2} m^* \omega_o^2 (x^2 + y^2) + \frac{1}{2m^*} p_z^2 + V_c(z), \quad (1)$$

in the Coulomb gauge, where ω_o is the characteristic frequency of the bare harmonic oscillator. The strain effect, which arises due to the lattice-mismatched hosts of the system and matters most for the phonon excitations, is virtually nonexistent on the collective excitations such as plasmons and

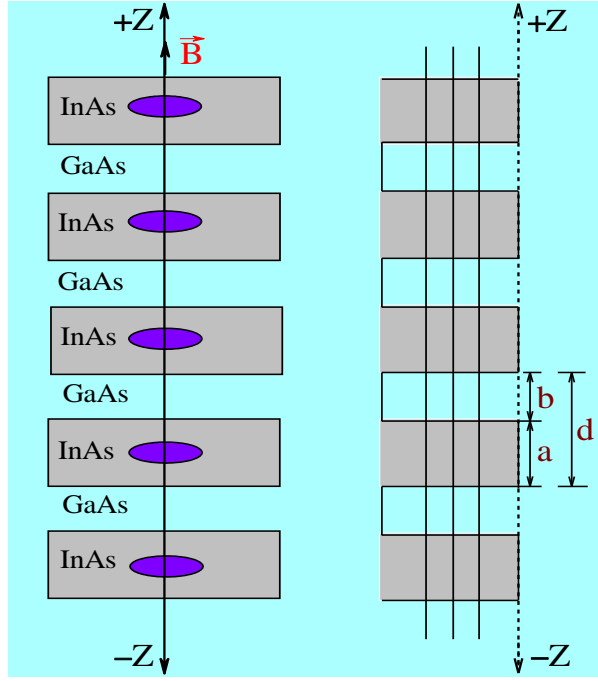


FIG. 1. (Color online) Schematics of the quantum wire made up of an infinitely periodic system of InAs islands separated by GaAs spacer layers (left panel). The grey (purple) area in the left panel refers to practically active region before (after) constraining the InAs islands with harmonic confinement in the x-y plane and the magnetic field in the symmetric gauge. The right panel shows the Kronig-Penney periodic-potential simulation along the growth direction. Here a (b) is the well (barrier) width and $d = a + b$ is the period of the resultant system making up the quantum wire. (After Kushwaha, Ref. 85).

magnetoplasmons. That is why we choose to exclude the strain effect from our theoretical framework. We ignore the spin-orbit interactions and the Zeeman energy for the sake of simplicity. Since the use of cylindrical polar coordinates seems to make more sense for the formal analysis, we cast the corresponding Schrodinger equation in the form

$$\left[-\frac{\hbar^2}{2m^*} \nabla_{\parallel}^2 - i\frac{\hbar}{2} \omega_c \partial_{\theta} + \frac{1}{8} m^* \Omega^2 r^2 \right] \Psi(r, \theta, z) - \left[\frac{\hbar^2}{2m^*} \partial_z^2 - V_c(z) \right] \Psi(r, \theta, z) = E \Psi(r, \theta, z), \quad (2)$$

where $\partial_x \equiv \partial/\partial x$, $\nabla_{\parallel}^2 = (\partial_r^2 + \frac{1}{r} \partial_r + \frac{1}{r^2} \partial_{\theta}^2)$, $\omega_c = eB/(m^*c)$ is the cyclotron frequency, and $\Omega = \sqrt{\omega_c^2 + 4\omega_0^2}$ the effective characteristic frequency of the dressed harmonic oscillator. Such a system as described above is solved by employing the method of separation of variables and formally characterized by the eigenfunction

$$\Psi(r, \theta, z) = \phi_n(r) \phi_m(\theta) \phi_k(z), \quad (3)$$

in the polar coordinates, where

$$\phi_n(r) = \frac{1}{\ell_e} \sqrt{\frac{(n+\alpha)!}{n!(\alpha!)^2}} e^{-y/2} y^{\alpha/2} \Phi(-n, \alpha+1, y), \quad (4)$$

$$\phi_m(\theta) = \frac{1}{\sqrt{2\pi}} e^{im\theta}, \quad (5)$$

$$\phi_k(z) = \frac{1}{\sqrt{N}} \sum_l e^{ikld} \chi_t(z - ld), \quad (6)$$

where $y = r^2/2\ell_e^2$, n is the subband index, $\alpha = |m|$, m being the orbital quantum number, $d = a + b$ the period, k the Bloch vector, $\ell_e = \sqrt{\hbar/m^*\Omega}$ the effective magnetic length, $\Phi(\dots)$ the confluent hypergeometric function [79], and $\chi_t(\dots)$ the Wannier function; and the eigenenergy

$$\epsilon_{nmk} = \left[n + \frac{1}{2}(\alpha + 1) \right] \hbar\Omega + \frac{1}{2}m\hbar\omega_c + \epsilon_t - \frac{W_t}{2} \cos(kd), \quad (7)$$

where ϵ_t is the energy of the t -th miniband and W_t is the band-width defined by

$$W_t = -4 \int_{-a/2}^{+a/2} dz \chi_t(z) V_0 \chi_t(z - d), \quad (8)$$

where we assume that the confining potential is a finite square well (Kronig-Penney potential) with a barrier height V_0 and well-width a . Since N (the number of quantum dot layers) is very large, the sum in Eq. (6) can be written as integral according to the replacement rule: $\sum_k \rightarrow (N/L_z) \int_{BZ} dk$. Eq. (6) represents the tight-binding constraint which hypothesizes a little overlap between the wave functions of different sites – with t as the miniband index. There $\chi_t(\dots)$, if normalized in the length of the lattice (or, nearly enough, in infinite length), satisfies: $\int dz \chi_t^*(z - nd) \chi_t(z - ld) = \delta_{nl}$ and $\int dz \phi_t^*(z) \phi_t(z) = 1$. Here $L_z = Nd$ is the total crystal length along the growth direction.

B. Generalized dielectric function

We start with the general expression of the non-interacting single-particle density-density response function (DDRF) $\chi^0(\dots)$ given by [1]

$$\chi^0(\mathbf{r}, \mathbf{r}'; \omega) = \sum_{ij} \Lambda_{ij} \psi_i^*(\mathbf{r}) \psi_j(\mathbf{r}) \psi_j^*(\mathbf{r}') \psi_i(\mathbf{r}'), \quad (9)$$

where $\mathbf{r} \equiv (\mathbf{r}_{\parallel}, z)$, with $\mathbf{r}_{\parallel} \equiv (r, \theta)$; the composite index $i, j \equiv k, n, t$; and Λ_{ij} is defined as follows.

$$\Lambda_{ij} = 2 \frac{f(\epsilon_i) - f(\epsilon_j)}{\epsilon_i - \epsilon_j + \hbar\omega^*}, \quad (10)$$

where $f(x)$ is the well-known Fermi distribution function. $\omega^* = \omega + i\gamma$ and small but nonzero γ represents the adiabatic switching of the Coulomb interactions in the remote past. The factor of 2 takes care of the spin degeneracy. Next, we make use of the Kubo's correlation function to write the induced particle density

$$n_{in}(\mathbf{r}; \omega) = \int d\mathbf{r}' \chi^0(\mathbf{r}, \mathbf{r}', \omega) V_{tot}(\mathbf{r}'; \omega) \quad (11)$$

$$= \int d\mathbf{r}' \chi(\mathbf{r}, \mathbf{r}', \omega) V_{ex}(\mathbf{r}'; \omega), \quad (12)$$

where $V_{tot} = V_{ex} + V_{in}$ is the total potential, with V_{ex} (V_{in}) as the external (induced) potential. χ and χ^o are, respectively, the total (or interacting) and single-particle DDRF and can be shown to be related with each other through the integral Dyson equation [see, e.g., Fig. 2]

$$\chi(\mathbf{r}, \mathbf{r}'; \omega) = \chi^0(\mathbf{r}, \mathbf{r}'; \omega) + \int d\mathbf{r}'' \int d\mathbf{r}''' \chi^0(\mathbf{r}, \mathbf{r}''; \omega) V_{ee}(\mathbf{r}'', \mathbf{r}''') \chi(\mathbf{r}''', \mathbf{r}'; \omega), \quad (13)$$

where $V_{ee}(\dots)$ stands for the binary Coulombic interactions in the direct space and is defined by

$$V_{ee}(\mathbf{r}, \mathbf{r}') = \frac{e^2}{\epsilon_b} \frac{1}{|\mathbf{r} - \mathbf{r}'|} = \frac{e^2}{\epsilon_b} \frac{1}{(|\mathbf{r}_{\parallel} - \mathbf{r}'_{\parallel}|)^2 + (z - z')^2 |^{1/2}}, \quad (14)$$

where ϵ_b the background dielectric constant of the system. Next, the induced potential in terms of the induced particle density is expressed as

$$V_{in}(\mathbf{r}, \omega) = \int d\mathbf{r}' V_{ee}(\mathbf{r}, \mathbf{r}') n_{in}(\mathbf{r}', \omega) \quad (15)$$

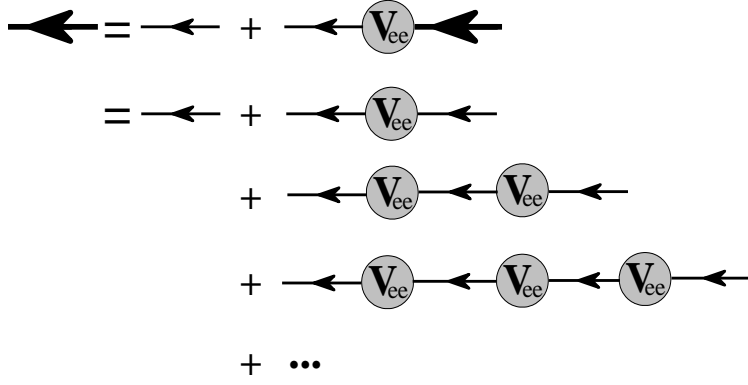


FIG. 2. A Feynman diagram for the Dyson equation: the thick [thin] line represents the total [single-particle] DDRF $\chi(\dots)$ [$\chi^o(\dots)$] within the full RPA [77]. Here V_{ee} represents the binary Coulombic interactions in the direct space. The arrows indicate the transition from initial to final spatio-temporal position of the particle in the interaction picture of the process.

This equation – with the aid of Eqs. (9) and (11) – can be cast in the following form:

$$\begin{aligned}
V_{in}(\mathbf{r}, \omega) &= \int d\mathbf{r}' \int d\mathbf{r}'' V_{ee}(\mathbf{r}, \mathbf{r}') \chi^0(\mathbf{r}', \mathbf{r}'', \omega) V_{tot}(\mathbf{r}'', \omega) \\
&= \sum_{i,j} \Lambda_{ij} \int d\mathbf{r}' \int d\mathbf{r}'' V_{ee}(\mathbf{r}, \mathbf{r}') \Psi_i^*(\mathbf{r}') \Psi_j(\mathbf{r}') \\
&\quad \times \Psi_j^*(\mathbf{r}'') \Psi_i(\mathbf{r}'') V_{tot}(\mathbf{r}'', \omega).
\end{aligned} \tag{16}$$

Making use of the explicit forms of the eigenfunctions in Eqs. (4)-(6) allows us to write Eq. (16) as

$$\begin{aligned}
V_{in}(\mathbf{r}_{\parallel}, \mathbf{z}; \omega) &= \frac{1}{\mathbf{N}^2} \sum_{nn'} \sum_{mm'} \sum_{tt'} \sum_{kk'} \sum_{ll'} \Lambda_{nn'tt'mm'}(k, k'; \omega) \\
&\quad \times \int d\mathbf{r}'_{\parallel} \int dz' \int d\mathbf{r}''_{\parallel} \int dz'' V_{ee}(\mathbf{r}_{\parallel}, \mathbf{r}'_{\parallel}; z - z') \\
&\quad \times \phi_{nm}^*(\mathbf{r}'_{\parallel}) \phi_{n'm'}(\mathbf{r}'_{\parallel}) \phi_{n'm'}^*(\mathbf{r}''_{\parallel}) \phi_{nm}(\mathbf{r}''_{\parallel}) \\
&\quad \times e^{-ikld} e^{ik'ld} e^{-ik'l'd} e^{ik'l'd} \\
&\quad \times \chi_t^*(z' - ld) \chi_t(z' - ld) \chi_t^*(z'' - l'd) \chi_t(z'' - l'd) \\
&\quad \times V_{tot}(\mathbf{r}''_{\parallel}, z''; \omega),
\end{aligned} \tag{17}$$

where $k' = k + q$, with q as the momentum transfer. Next, we (i) multiply both sides of this equation by $e^{-iq'z}$ and integrate with respect to z and (ii) introduce, for convenience, a single Fourier component of $V_{tot}(\dots)$ to write $V_{tot}(\mathbf{r}_{\parallel}, z; \omega) = e^{iq'z} V_{tot}(\mathbf{r}_{\parallel}, q'; \omega)$. So, let us first rewrite Eq. (17) in clearer terms before we open up the sums over ll' and kk' . After rearranging a few terms, Eq. (17) thus assumes

the following form.

$$\begin{aligned}
V_{in}(\mathbf{r}_{\parallel}, q'; \omega) &= \frac{1}{N^2} \sum_{nn'} \sum_{mm'} \sum_{tt'} \sum_{kk'} \sum_{ll'} \Lambda_{nn'mm'}^{tt'll'}(k, k'; \omega) \\
&\times \int d\mathbf{r}'_{\parallel} V_{ee}(\mathbf{r}_{\parallel} - \mathbf{r}'_{\parallel}; q') \phi_{nm}^*(\mathbf{r}'_{\parallel}) \phi_{n'm'}(\mathbf{r}'_{\parallel}) \\
&\times \int d\mathbf{r}''_{\parallel} \phi_{n'm'}^*(\mathbf{r}''_{\parallel}) V_{tot}(\mathbf{r}''_{\parallel}, z''; \omega) \phi_{nm}(\mathbf{r}''_{\parallel}) \\
&\times e^{iqld} e^{-iq'l'd} e^{-iq'l'd} e^{iq'l'd} \\
&\times \int dz' e^{-iq'(z'-ld)} \chi_t^*(z'-ld) \chi_{t'}(z'-ld) \\
&\times \int dz'' e^{iq'(z''-l'd)} \chi_t(z''-l'd) \chi_{t'}^*(z''-l'd), \tag{18}
\end{aligned}$$

where the Fourier-transformed Coulombic interaction

$$V_{ee}(\mathbf{r}_{\parallel} - \mathbf{r}'_{\parallel}; q') = \frac{2e^2}{\epsilon_b} K_0(q' |\mathbf{r}_{\parallel} - \mathbf{r}'_{\parallel}|), \tag{19}$$

where $K_0(\dots)$ is the zeroth-order modified Bessel function of the second kind. Since the last two integrals in Eq. (18) can very well be jointly written as

$$S_{tt'}(q) = \left| \int dz e^{-iqz} \chi_t^*(z) \chi_{t'}(z) \right|^2, \tag{20}$$

we obtain, from the sum over l' ,

$$\frac{1}{N} \sum_{l'} e^{i(q'-q)(l'-l)d} = \frac{1}{Nd} \int d(l'd) e^{i(q'-q)(l'-l)d} = \frac{1}{L_z} 2\pi \delta(q - q'), \tag{21}$$

and the remaining sum over l simplifies to $\frac{1}{N} \sum_l 1 = 1$. As a result, the sum over k' solves as follows:

$$\begin{aligned}
\frac{2\pi}{L_z} \sum_{k'} \Lambda_{nn'mm'}^{tt'}(k, k'; \omega) \delta(q - q') &= \int dk' \Lambda_{nn'mm'}^{tt'}(k, k'; \omega) \delta(k' - k - q') \\
&= \Lambda_{nn'mm'}^{tt'}(k, k' = k + q'; \omega). \tag{22}
\end{aligned}$$

Next, we make use of the substitution

$$\Pi_{nn'mm'tt'}(k, k'; \omega) = \sum_k \Lambda_{nn'mm'}^{tt'}(k, k' = k + q'; \omega), \tag{23}$$

and replace q' safely by q everywhere. As such, Eq. (18), with the aid of Eqs. (19)-(23), becomes

$$\begin{aligned}
V_{in}(\mathbf{r}_{\parallel}, q; \omega) &= \frac{2e^2}{\epsilon_b} \sum_{nn'} \sum_{mm'} \sum_{tt'} \Pi_{nn'mm'tt'}(k, k'; \omega) \\
&\quad \times \int d\mathbf{r}'_{\parallel} K_0(q|\mathbf{r}_{\parallel} - \mathbf{r}'_{\parallel}|) \phi_{nm}^*(\mathbf{r}'_{\parallel}) \phi_{n'm'}(\mathbf{r}'_{\parallel}) \\
&\quad \times \langle n'm' | V_{tot}(\mathbf{r}''_{\parallel}, q; \omega) | nm \rangle S_{tt'}(q).
\end{aligned} \tag{24}$$

Now, we take matrix elements of both sides of this equation within the states $|ij\rangle$ and $|i'j'\rangle$ to write

$$\begin{aligned}
\langle ij | V_{in}(\mathbf{r}_{\parallel}, q; \omega) | i'j' \rangle &= \sum_{nn'} \sum_{mm'} \sum_{tt'} \Pi_{nn'mm'tt'}(k, k'; \omega) U_{ij,i'j',nm,n'm'}(q) S_{tt'}(q) \\
&\quad \times \langle n'm' | V_{tot}(\mathbf{r}''_{\parallel}, q; \omega) | nm \rangle,
\end{aligned} \tag{25}$$

where the matrix elements of the Coulombic interactions

$$U_{ij,i'j',nm,n'm'}(q) = \frac{2e^2}{\epsilon_b} \int d\mathbf{r}_{\parallel} \int d\mathbf{r}'_{\parallel} \phi_{ij}^*(\mathbf{r}_{\parallel}) \phi_{i'j'}(\mathbf{r}_{\parallel}) K_0(q|\mathbf{r}_{\parallel} - \mathbf{r}'_{\parallel}|) \phi_{n'm'}^*(\mathbf{r}'_{\parallel}) \phi_{nm}(\mathbf{r}'_{\parallel}). \tag{26}$$

Before we proceed further, let us define a few composite indices such as $\mu \equiv n, m$; $\mu' \equiv n', m'$; $\nu \equiv i, j$; and $\nu' \equiv i', j'$ in order to rewrite Eq. (25) in the form

$$\langle \nu | V_{in}(\mathbf{r}_{\parallel}, q; \omega) | \nu' \rangle = \sum_{\mu\mu'} \sum_{tt'} \Pi_{\mu\mu'tt'}(k, k'; \omega) U_{\nu\nu'\mu\mu'}(q) S_{tt'}(q) \langle \mu' | V_{tot}(\mathbf{r}''_{\parallel}, q; \omega) | \mu \rangle, \tag{27}$$

where

$$U_{\nu\nu'\mu\mu'}(q) = \frac{2e^2}{\epsilon_b} \int d\mathbf{r}_{\parallel} \int d\mathbf{r}'_{\parallel} \phi_{\nu}^*(\mathbf{r}_{\parallel}) \phi_{\nu'}(\mathbf{r}_{\parallel}) K_0(q|\mathbf{r}_{\parallel} - \mathbf{r}'_{\parallel}|) \phi_{\mu'}^*(\mathbf{r}'_{\parallel}) \phi_{\mu}(\mathbf{r}'_{\parallel}). \tag{28}$$

Now, we invoke the condition of self-consistency – $V_{tot} = V_{ex} + V_{in}$ – to rewrite Eq. (27)

$$\begin{aligned}
\langle \nu | V_{ex}(\mathbf{r}_{\parallel}, q; \omega) | \nu' \rangle &= \sum_{\mu\mu'} \left[\delta_{\mu\nu} \delta_{\mu'\nu'} - \sum_{tt'} \Pi_{\mu\mu'tt'}(k, k'; \omega) U_{\nu\nu'\mu\mu'}(q) S_{tt'}(q) \right] \\
&\quad \times \langle \mu' | V_{tot}(\mathbf{r}''_{\parallel}, q; \omega) | \mu \rangle.
\end{aligned} \tag{29}$$

Here $\delta_{\mu\nu}$ is the Kronecker delta. Since the external potential and the total potential are correlated through the nonlocal, dynamic dielectric function $\epsilon(\dots)$ such that

$$V_{ex}(\mathbf{r}_{\parallel}, q; \omega) = \int d\mathbf{r}'_{\parallel} \epsilon(\mathbf{r}_{\parallel}, \mathbf{r}'_{\parallel}, q; \omega) V_{tot}(\mathbf{r}'_{\parallel}, q; \omega). \quad (30)$$

By taking the matrix elements of the left-hand side of this equation between the states $|\nu\rangle$ and $|\nu'\rangle$ and adjusting a few terms, we obtain

$$\begin{aligned} \langle \nu | V_{ex}(\dots) | \nu' \rangle &= \sum_{\mu} \sum_{\mu'} \langle \mu \nu | \epsilon(\dots) | \nu' \mu' \rangle \langle \mu' | V_{tot}(\dots) | \mu \rangle \\ &= \sum_{\mu \mu'} \epsilon_{\mu \nu \mu' \nu'}(\dots) \langle \mu' | V_{tot}(\dots) | \mu \rangle. \end{aligned} \quad (31)$$

A piecewise comparison of Eqs. (29) and (31) leaves us with the following:

$$\epsilon_{\mu \nu \mu' \nu'}(q, \omega) = \delta_{\mu \nu} \delta_{\mu' \nu'} - A_{\mu \mu'}(q, \omega) U_{\nu \nu' \mu \mu'}(q), \quad (32)$$

where

$$A_{\mu \mu'}(q, \omega) = \sum_{tt'} \Pi_{\mu \mu'}(k, k' = k + q; \omega) \cdot S_{tt'}(q) \quad (33)$$

Equation (32) represents the generalized (nonlocal, dynamic) dielectric function for the system subjected to a lateral confining harmonic potential and an applied magnetic field in the symmetric gauge. This is the main result, which can be exploited to study a whole host of electronic, optical, and transport phenomena in the system. However, the generalized dielectric function needs to be specified in order to make an otherwise impractical $(\infty \times \infty)$ matrix – generated from Eq. (32) – docile.

C. The KP, Wannier, and Bloch functions

Let us briefly recall how the Wannier, Bloch, and KP functions are so tightly interwoven. The Wannier function of a band $\chi_t(z - z_n)$ is expressed in terms of the Bloch function $\phi_k(z)$ of the same band such that

$$\chi_t(z - z_n) = \frac{1}{\sqrt{N}} \sum_k e^{-ikz_n} \phi_k(z), \quad (34)$$

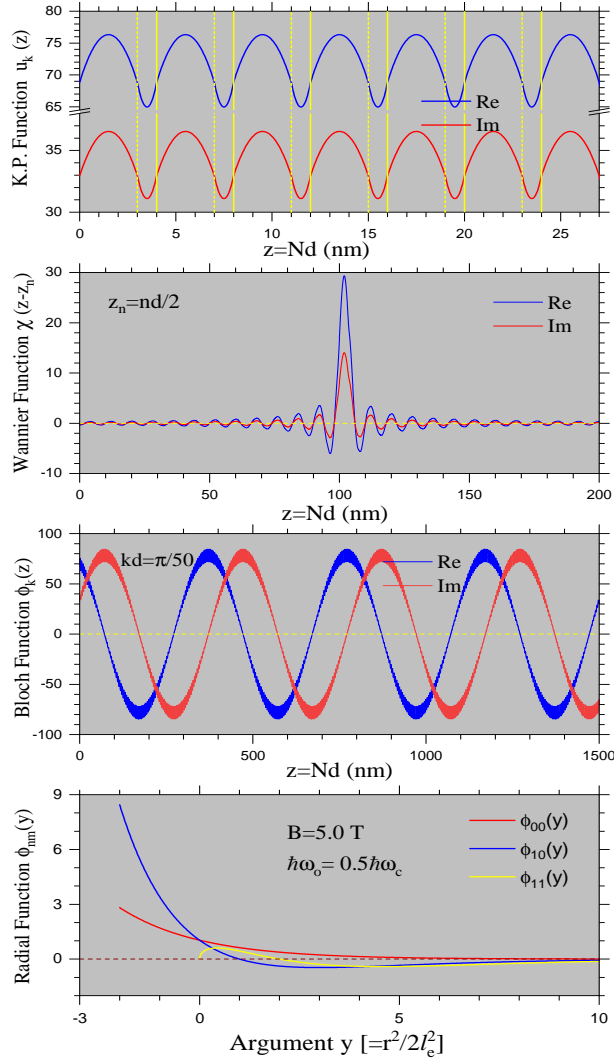


FIG. 3. (Color online) Graphic behavior of the KP, the Wannier, the Bloch, and the Laguerre functions as used in this work. The well (barrier) thickness is 3 (1) nm and $V_0 = 349.11$ meV. The other parameters are as listed in the respective panels.

where the Bloch function $\phi_k(z)$ is defined in terms of the KP function $u(z)$ as

$$\phi_k(z) = e^{ikz} u(z), \quad (35)$$

where $u(z) = u(z + d)$ satisfies the Schrodinger equation

$$\left[-\frac{\hbar^2}{2m^*} \frac{d^2}{dz^2} + V_c(z) \right] u(z) = \epsilon_z u(z). \quad (36)$$

The Wannier function $\chi_t(\dots)$ in Eq. (34) – with the aide of Eq. (35) – assumes the form

$$\chi_t(z - z_n) = \frac{1}{\sqrt{N}} \sum_k e^{ik(z-z_n)} u(z) = \sqrt{N} u(z) \frac{\sin[\pi(z - z_n)/d]}{[\pi(z - z_n)/d]}. \quad (37)$$

The Wannier functions and the Bloch functions satisfy the orthonormalization conditions just as explained in the text following Eq. (8) above. Since the general (total) eigenfunction characterizing the system is expressed in terms of these functions, we choose to illustrate their individual behavior [see Fig. 3]. As each panel reaffirms the exact behavior of the respective function, we safely avoid expanding on the discussion since *a picture is worth a thousand words*.

D. The functional strategy: Specification

As stated above, the generalized dielectric function (GDF) requires certain specifications to be met before it can be exploited to obtain desired results such as the excitation spectrum of the system. First, we would like to underline the z-motion along the superlattice axis (and the associated factors), which – due, in fact, to the very nature of the Lorentz force – remains unaffected by the applied magnetic field (B) because $\mathbf{B} \parallel \hat{z}$. The immediate relevance of the z-motion in the present system involves, for example, the miniband structure, the bandwidth, and the overlap factor of $S_{t'}$ (q). Let us limit ourselves *once and for all* to the lowest miniband structure – i.e., $t = 0 = t'$ – for the sake of simplicity. In order to understand the miniband structure we make use of the well-known Bastard's boundary conditions (BBC) because the active and inactive layers in the 1D superlattice system are made up of different host materials [80]. Notice that we have already studied the details of the miniband structure (due to the KP potential model) and the behavior of the overlap factor $S_{00}(q)$ in the zero-field case [62] and hence do not feel an urge to expand on them here. Similarly, we had also discussed there the critical connection between the symmetry (of the confining 2D harmonic potential) and the degeneracy in sufficient detail.

Now, we move on to discuss the necessary specification in the case of a non-zero magnetic field. Given that most of the experiments on the low-dimensional systems are performed at lower temperatures, we limit ourselves to the absolute zero (i.e., $T = 0$ K). In this regard, we believe that the temperature dependence of our results would be significant only at $T \gtrsim 35$ K. The absolute zero allows us to replace the Fermi distribution function with the Heaviside unit step function such that

$$f(\epsilon) = \theta(\epsilon_F - \epsilon) = \begin{cases} 1 & \text{if } \epsilon_F > \epsilon \\ 0 & \text{if } \epsilon_F < \epsilon \end{cases}, \quad (38)$$

where ϵ_F is the Fermi energy in the system. The next important point is the subband occupancy, which is implicit in the suffix $\mu, \mu', \nu,$ and ν' in Eq. (32), for example. The GDF in Eq. (32) represents, in general, an $\infty \times \infty$ matrix until and unless we delimit the number of subbands and hence the electronic transitions to be considered in the problem. While experiments may report multiple subbands occupied, theoretically it is vastly difficult to compute the excitation spectrum for the multiple-subband model – i.e., when n ($-n < m < +n$) is a very big number. The real reason is that the GDF turns out to be a matrix of the dimension of $\eta^2 \times \eta^2$, where η is the number of subbands accounted for in the problem. Tackling such enormous matrices (for a large η) analytically is a *hard nut to crack*, which is why we choose to confine ourselves to a two-subband model ($n, n' \equiv 1, 2$) with only the lowest one occupied and keep the complexity to a minimum. This is quite a sensible assumption for the small-density, low-dimensional systems at lower temperatures where most of the experiments are performed. As such, the GDF in Eq. (32) can be cast in the form:

$$\tilde{\epsilon}(q, \omega) = \begin{bmatrix} 1 - B_{0000}^{mm'jj'} & -B_{0001}^{mm'jj'} & -B_{0010}^{mm'jj'} & -B_{0011}^{mm'jj'} \\ -B_{0100}^{mm'jj'} & 1 - B_{0101}^{mm'jj'} & -B_{0110}^{mm'jj'} & -B_{0111}^{mm'jj'} \\ -B_{1000}^{mm'jj'} & -B_{1001}^{mm'jj'} & 1 - B_{1010}^{mm'jj'} & -B_{1011}^{mm'jj'} \\ -B_{1100}^{mm'jj'} & -B_{1101}^{mm'jj'} & -B_{1110}^{mm'jj'} & 1 - B_{1111}^{mm'jj'} \end{bmatrix}, \quad (39)$$

where $B_{nn'ii'}^{mm'jj'} = A_{nn'}^{mm'} U_{nn'ii'}^{mm'jj'}$ and $A_{nn'}^{mm'} = \Pi_{nn'}^{mm'}(k, k' = k + q; \omega) \cdot S_{00}(q)$. Since subband index n can take the value zero, we have specified $n, n' \equiv 0, 1$ – rather than $n, n' \equiv 1, 2$. The superscripts refer to the orbital quantum numbers, which are defined such that $-n < m < +n$. Finally, it is imperative to realize that the symmetry of the confining *harmonic* potential in the system brings in some persuasive consequences. For a symmetric potential well, U_{ijkl} (the Fourier-transformed Coulomb interaction) is strictly zero for an arbitrary value of q if the sum $i + j + k + l$ is an *odd* number. This is because the analogous eigenfunction is either symmetric or antisymmetric under space reflection. This scenario is perfectly clear in the zero-field case ($B = 0$). For a finite B , the situation takes twists and turns due to the fact that the center of the harmonic oscillator is displaced from zero due to the cyclotron orbits by a finite distance on the order of $x_c (= q\ell_e^2)$. However, a heedful mathematical manipulation of the integrands is all that is merely required to prove that U_{ijkl} is virtually zero even when $B \neq 0$, provided that the sum $i + j + k + l$ is odd. The unoccupancy of the second subband and the symmetry

of the confining potential thus allow the matrix in Eq. (39) to assume the form

$$\tilde{\epsilon}(q, \omega) = \left(1 - B_{0000}^{0000}\right) \times \begin{bmatrix} 1 - B_{0101}^{0-10-1} & -B_{0101}^{0-100} & -B_{0101}^{0-101} & -B_{0110}^{0-1-10} & -B_{0110}^{0-100} & -B_{0110}^{0-110} \\ -B_{0101}^{0+00-1} & 1 - B_{0101}^{0+000} & -B_{0101}^{0+001} & -B_{0110}^{0+0-10} & -B_{0110}^{0+000} & -B_{0110}^{0+010} \\ -B_{0101}^{0+10-1} & -B_{0101}^{0+100} & 1 - B_{0101}^{0+101} & -B_{0110}^{0+1-10} & -B_{0110}^{0+100} & -B_{0110}^{0+110} \\ -B_{1001}^{-100-1} & -B_{1001}^{-1000} & -B_{1001}^{-1001} & 1 - B_{1010}^{-10-10} & -B_{1010}^{-1000} & -B_{1010}^{-1010} \\ -B_{1001}^{+000-1} & -B_{1001}^{+0000} & -B_{1001}^{+0001} & -B_{1010}^{+00-10} & 1 - B_{1010}^{+0000} & -B_{1010}^{+0010} \\ -B_{1001}^{+100-1} & -B_{1001}^{+1000} & -B_{1001}^{+1001} & -B_{1010}^{+10-10} & -B_{1010}^{+1000} & 1 - B_{1010}^{+1010} \end{bmatrix} \quad (40)$$

A word of warning: the superscripts of the elements merely refer to the plus or minus of the respective indices without using a comma in between (for brevity). The same plus or minus in front of some zeros are added only for the sake of *spatial* symmetry of the elements. Now, we simplify the matrix in Eq. (40) by following the usual rules of matrix arithmetic. So, let us subtract the 3rd column from the 1st and the 6th column from the 4th to write the resulting matrix, which is further simplified by subtracting 3rd row from the 1st and the 6th row from the 4th to finally write

$$\tilde{\epsilon}(q, \omega) = \left(1 - B_{0000}^{0000}\right) \times \begin{bmatrix} 2 & 0 & -1 & 0 & 0 & 0 \\ 0 & 1 - B_{0101}^{0+000} & -B_{0101}^{0+001} & 0 & -B_{0110}^{0+000} & -B_{0110}^{0+010} \\ -1 & -B_{0101}^{0+100} & 1 - B_{0101}^{0+101} & 0 & -B_{0110}^{0+100} & -B_{0110}^{0+110} \\ 0 & 0 & 0 & 2 & 0 & -1 \\ 0 & -B_{1001}^{+0000} & -B_{1001}^{+0001} & 0 & 1 - B_{1010}^{+0000} & -B_{1010}^{+0010} \\ 0 & -B_{1001}^{+1000} & -B_{1001}^{+1001} & -1 & -B_{1010}^{+1000} & 1 - B_{1010}^{+1010} \end{bmatrix} \quad (41)$$

In obtaining Eq. (41), the double operations (as stated above) have also taken advantage of the fact that the terms of the form of $A_{01}^{0,-1}[U_{0101}^{0,-1,0,-1} - U_{0101}^{0,-1,0,1}]$ vanish. This is because the square brackets yield the integrands of the Coulomb matrix elements, which differ only in the signs of the sine terms, make the integrands odd, and hence become zero. Since the collective excitations in a system are obtained by searching the zeros of the determinant of $\tilde{\epsilon}(\dots)$, we obtain

$$\left(1 - B_{0000}^{0000}\right) \left[1 - \left(B_{0101}^{0000} + B_{1010}^{0000}\right) - [2] \left(B_{0101}^{0101} + B_{1010}^{1010}\right)\right] = 0 \quad (42)$$

after the straightforward but lengthy mathematical steps. Another appealing and engaging way of

writing Eq. (42) is as follows:

$$(1 - A_{00}^{00} U_{0000}^{0000}) \left[1 - C_{01}^{00} U_{0101}^{0000} - [2] C_{01}^{01} U_{0101}^{0101} \right] = 0 \quad (43)$$

where

$$A_{00}^{00} = \Pi_{00}^{00} S_{00}(q), \quad (44)$$

$$C_{01}^{00} = A_{01}^{00} + A_{10}^{00} = \chi_{01}^{00} S_{00}(q), \quad (45)$$

$$C_{01}^{01} = A_{01}^{01} + A_{10}^{10} = \chi_{01}^{01} S_{00}(q), \quad (46)$$

where $\chi_{01}^{00} = \Pi_{01}^{00} + \Pi_{10}^{00}$ and $\chi_{01}^{01} = \Pi_{01}^{01} + \Pi_{10}^{01}$. Notice that Π_{00}^{00} and $\chi_{01}^{mm'}$ refer, respectively, to the intrasubband and intersubband electronic transitions. Equation (43) is actually the one which is treated at the computational level for all practical purposes. It is interesting to note that in spite of the substantial complexity brought about by the applied magnetic field, the intrasubband and the intersubband excitations making up the complete excitation spectrum of the system are observed to be clearly decoupled. The explicit expressions of the matrix elements of the Coulombic interactions $U_{nn'ii'}^{mm'jj'}$ required in Eq. (43) will be listed in the next section.

E. The Long wavelength limit

Given their importance, it is interesting to study the long wavelength limit (LWL) of the polarizability functions such as Π_{00}^{00} , χ_{01}^{00} , and χ_{01}^{01} involved in the process. To that end, the required mathematical diagnosis is quite complex and lengthy, which is why we choose to outline the procedure briefly and thereby restrain the length of the article. We begin with writing $\Pi_{nn'}^{mm'}$ at absolute zero, replace the sum over k with an integral – having the upper (lower) limit as k_F ($-k_F$) – using the proper replacement rule, solve the integral with the help of § 2.558.4 on page 183 in GR (1994) in Ref. [79], simplify the result of the integral using $\tanh^{-1}(x) = \frac{1}{2} \ln \left[\frac{1+x}{1-x} \right]$, and then finally writing the series expansion of $\ln(1+x)$ in the limit of $x \ll 1$. Next, we already know that $\chi_{nn'}^{mm'} = \Pi_{nn'}^{mm'} + \Pi_{n'n}^{m'm}$, so it becomes less cumbersome to write directly $\chi_{nn'}^{mm'}$ for the specific values of the suffixes. The result is

$$\Pi_{00}^{00} \simeq \frac{n_{1D} q^2}{m^* \omega^2} + O(q^2), \quad \text{for } n = 0 = n' \text{ and } m = 0 = m', \quad (47)$$

where $m^* [= \hbar^2/(w_h d^2); w_h = W_0/2]$, for the intrasubband excitations and

$$\chi_{01}^{00} \simeq \frac{2 n_{1D} \epsilon_{00}}{[(\hbar\omega)^2 - (\epsilon_{00})^2]} + O(q), \quad \epsilon_{00} = \hbar\Omega; \quad \text{for } m = 0 = m' \quad (48)$$

$$\chi_{01}^{01} \simeq \frac{2 n_{1D} \epsilon_{01}}{[(\hbar\omega)^2 - (\epsilon_{01})^2]} + O(q), \quad \epsilon_{01} = -\frac{3}{2} \hbar\Omega - \frac{1}{2} \hbar\omega_c; \quad \text{for } m = 0, m' = +1 \quad (49)$$

for the intersubband excitations. Equations (47)–(49) clearly attest the fact that the long wavelength limits of the polarizability functions are independent of the virtual dimensionality of the system and have the same forms for higher dimensions [1].

F. The density of states

The knowledge of the density of states (DOS) is of paramount significance in many areas of physics and helps us explain numerous classical and quantal phenomena in a given system. For instance, the zero, vanishingly low, and the high DOS indicate, respectively, the gap, the psuedo-gap, and the free propagation of the respective wave in the system. This implies that the computation of the DOS can (and does) help us in studying the band-gap engineering in a system. The photonic and phononic crystals are the recent examples where the band-gap engineering played a crucial role in defining their specific use and in making them two of the hottest topics in physics during the past three decades. The DOS – $D(\epsilon)$ – in the systems of diminishing dimensions is in essence the number of distinct states at a certain energy level that electrons are allowed to fill and is one such inceptive feature of a system that clearly demonstrates the dimensional dependence. The standard analytical diagnosis divulges that $D(\epsilon) \propto \epsilon^{1/2}$, $D(\epsilon) \propto \epsilon^0$, and $D(\epsilon) \propto \epsilon^{-1/2}$, respectively, in the 3D, 2D, and 1D systems. In the extreme case of quantum confinement – such as quantum dot systems – the DOS is known to be δ –function-like inferring to the vanishing of thermal broadening [1]. We have derived the DOS for the present system on the basis of the single-particle energy in Eq. (7) and the result is

$$D(\epsilon) = \frac{2}{\pi d} \sum_{nm} \left[w_h^2 - (\epsilon - \epsilon_{nmt})^2 \right]^{-1/2} \cdot \theta \left(w_h^2 - (\epsilon - \epsilon_{nmt})^2 \right) \quad (50)$$

where $\theta(\dots)$ is the Heaviside step function and the symbol ϵ_{nmt} is defined as

$$\epsilon_{nmt} = \left[n + \frac{1}{2}(\alpha + 1) \right] \hbar\Omega + \frac{1}{2} m \hbar\omega_c + \epsilon_t \quad (51)$$

Figure 4 shows the computed DOS versus the excitation energy for a given value of the magnetic

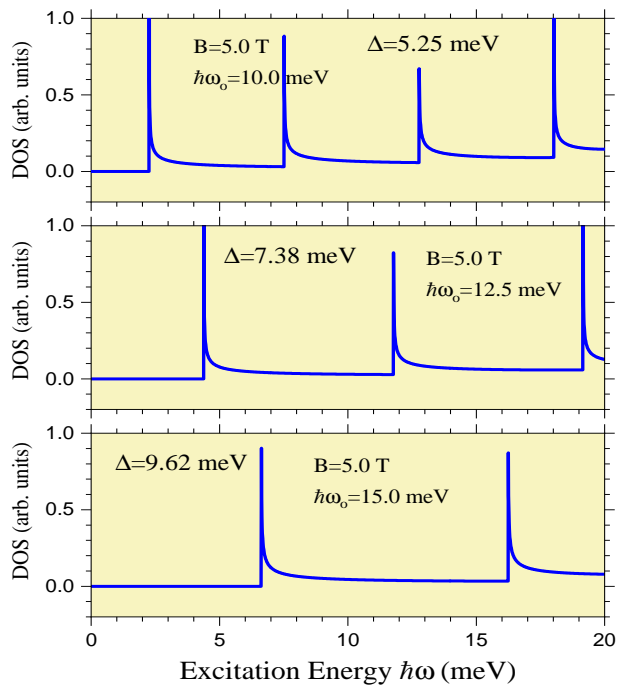


FIG. 4. (Color online) The density of states vs. the excitation energy for the VSQD system, for a magnetic field of $B = 5.0$ T. The confinement potential is defined as $\hbar\omega_o = 10.0$ meV (top panel), 12.5 meV (middle panel), and 15.0 meV (bottom panel). The band-width is $W_0 = 19.76$ meV.

field. Since the magnetic field is constant, it is only the confinement potential that influences the shifting of the spikes in the three panels. We observe that the DOS spikes start isolating from each other with increasing confinement potential. This process clearly results in diminishing the number of spikes within a given energy range. In the simpler situations, it is the subband spacing that defines the gap between the two consecutive spikes in the DOS. But, it is not the case with the present periodic system of the VSQD. It is evident from three panels that the number of DOS spikes reduce with increasing confinement. This tendency is found to obey a simple mathematical rule: $n_f = \text{Int}[n_i \times (\Omega_i/\Omega_f)]$, where n_j is the number of peaks and Ω_j is the effective characteristic frequency of the harmonic oscillator; $j \equiv i, f$. To be specific, the subindex $i(f)$ refers to the initial (final) case of the history. This empirical rule was discovered in the case of a realistic quantum wire where it remains unfaillingly true both with and without an applied magnetic field [1].

Figure 5 shows the density of states versus the excitation energy for a given value of the confinement potential. The magnetic field is defined as $B = 5.0$ meV (top panel), 6.0 meV (middle panel), and 7.0 meV (bottom panel). We observe that the DOS peaks start shifting towards the higher energy, but the energy separation between them becomes smaller with increasing magnetic field. For $B = 0$, it was found that while the DOS peaks shift towards higher energy, they start distancing from each other with increasing confinement potential [62]. This implies that the role of an applied magnetic

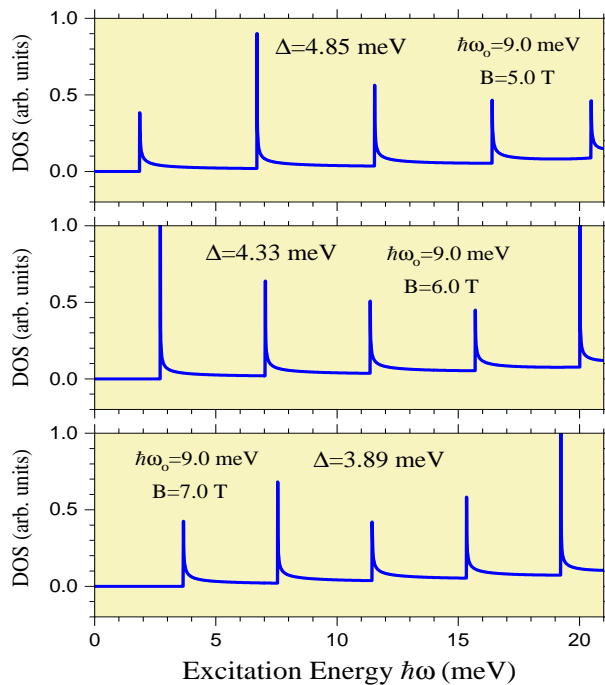


FIG. 5. (Color online) The density of states vs. the excitation energy for the VSQD system, for a confinement potential of $\hbar\omega_o = 9.0$ meV. The magnetic field is defined as $B = 5.0$ T (top panel), 6.0 T (middle panel), and 7.0 T (bottom panel). The band-width is $W_0 = 19.76$ meV. (After Kushwaha, Ref. 85).

field is virtually more than just to boost the confinement. In the case of realistic quantum wires, we have noticed similar behavior regarding the peaks' shifting, but the DOS peaks experience larger energy separation with increasing magnetic field [1]. The empirical rule deduced in relation with Fig. 4 does not hold good in this case (for the set of parameters used), whereas it remains valid for the realistic quantum wires (both for $B = 0$ and $B \neq 0$) [1]. We think that the moderate confinement – with $B \neq 0$ – favors the VSQD in mimicking a realistic quantum wire.

Figure 6 displays the DOS as a function of the excitation energy for a typical magnetic field but an extremely strong confinement potential. A too strong lateral (2D) confinement seems to bring the system of VSQD to a standstill by causing disruption and thereby decoupling the InAs islands holding the quantum dots. This implies that the system in this situation is clearly not anticipated to mimic the quantum wire. Interestingly, every (still broadened) spike is seen to be made up of $2n'$ spikes and centered at the confinement harmonics ($n' \cdot \hbar\omega_o$). This is intelligible: given that $\omega_o \gg \omega_c$, Eq. (51) simplifies to $\epsilon_{nmt} = n' \cdot \hbar\omega_o$, with $n' \equiv 2[(n + \frac{1}{2}(|m| + 1))]$; which implies that the average width of the spikes at every harmonic is given by $\Delta = W_0$. This is exactly what we observe in the picture (see the double-headed arrows in magenta).

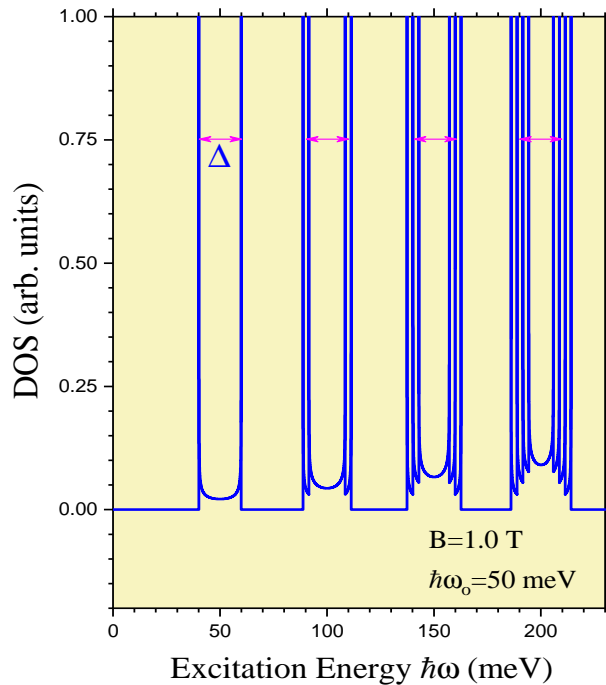


FIG. 6. (Color online) The density of states vs. the excitation energy for the VSQD system, for a magnetic field of $B = 1.0$ T and the confinement potential $\hbar\omega_0 = 50.0$ meV. The band-width is $W_0 = 19.76$ meV. The double headed arrows (in magenta) refer to the average width $\Delta = W_0$.

G. The Fermi energy

The textbooks on Condensed Matter Physics teach us the terms like Fermi gas, Fermi energy, Fermi level, Fermi surface, Fermi temperature, and Fermi velocity, which are so closely associated with the spin-1/2 particles called fermions. The Fermions are governed by the Pauli exclusion principle and they obey the Fermi-Dirac statistics. A precise knowledge of these terms and of the distinction between them is vital to the understanding of electron dynamics of a quantum system. We would like to highlight three of them: Fermi surface, which is defined as the Fermi-energy surface in the reciprocal space; Fermi energy, which is the energy difference between the highest and lowest occupied states in a system of non-interacting fermions at absolute zero; and Fermi level, which is the total energy level (including kinetic and potential energies) that remains well-defined even in the complex interacting system at thermodynamic equilibrium. Here, we are interested in the Fermi energy since we deal with the system that lies at absolute zero. The Fermi energy derived on the basis of the single-particle energy in Eq. (7) is expressed as

$$n_{1D} = \frac{2}{\pi d} \sum_{nm} \cos^{-1} \left[-\frac{1}{w_h} (\epsilon_F - \epsilon_{nmt}) \right] \cdot \theta \left[-\frac{1}{w_h} (\epsilon_F - \epsilon_{nmt}) \right] \quad (52)$$

where n_{1D} is the linear charge density of the electrons in the system. This is exactly the formula we make use of to compute the Fermi energy for various instances.

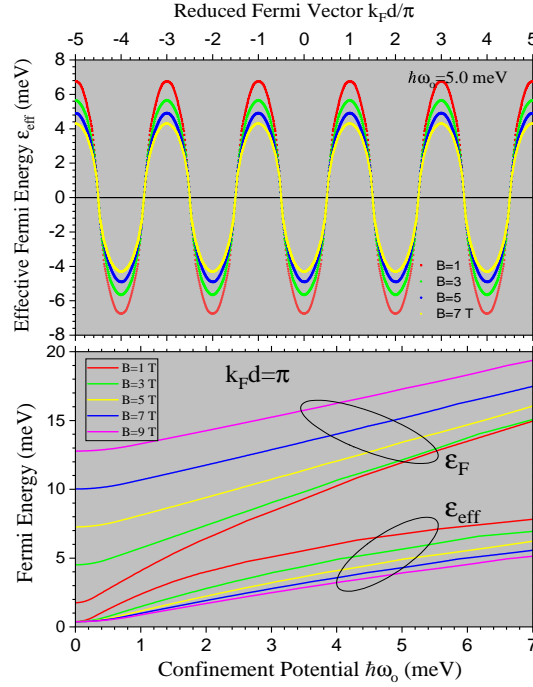


FIG. 7. (Color online) Upper panel: The effective Fermi energy vs. the reduced Fermi vector, for confinement potential $\hbar\omega_o = 5.0$ meV and for several values of the magnetic field. We purposely made this choice to have $k_F d$ on the abscissa – it could very well be the charge density n_{1D} . Lower panel: The Fermi energy vs. the confinement potential, for a specific value of k_F and for several values of B . The lower (upper) set of curves refers to the effective Fermi (Fermi) energy in the system. The band-width $W_0 = 19.76$ meV.

The upper panel of Figure 7 illustrates the *effective* Fermi energy as a function of the reduced Fermi vector ($k_F d / \pi$) for a given value of the confinement potential $\hbar\omega_o$ and for several values of the magnetic field B . The effective Fermi energy ϵ_{eff} is defined as $\epsilon_{eff} = \epsilon_F - \frac{1}{2} \hbar\Omega$. Notice that ϵ_{eff} oscillates as a function of the Fermi vector k_F , for any value of magnetic field. This oscillatory behavior is an outright reflection of the cosine term in the single-particle energy due to the tight-binding approximation [see Eq. (7)]. Interestingly, the peak-to-peak amplitude of ϵ_{eff} decreases with increasing B . This is clearly comprehensible and follows the fact that the cyclotron radius $r_c \propto B^{-1}$. The abscissa in Fig. 7 can also account for the linear charge density in the system, since the Fermi vector is related to the 1D charge density by a simple relation: $k_F = (\pi/2)n_{1D}$. The lower panel shows the Fermi energy ϵ_F as well as the effective Fermi energy ϵ_{eff} as a function of the confinement potential $\hbar\omega_o$, for a given value of the Fermi vector k_F and for several values of the magnetic field B . The lower panel can very well be considered complementary to the upper one as it substantiates the trend of ϵ_{eff} in the latter for any value of $\hbar\omega_o$. The knowledge of the Fermi energy is central to the understanding of nearly all electronic, optical, and transport properties of a quantal system at a given

temperature. The transport properties – such as conductance or resistance – are true reflections of the electron dynamics at the Fermi surface. What is so captivating about the Fermi surface is that it can be tailored before it tailors the rest in the system.

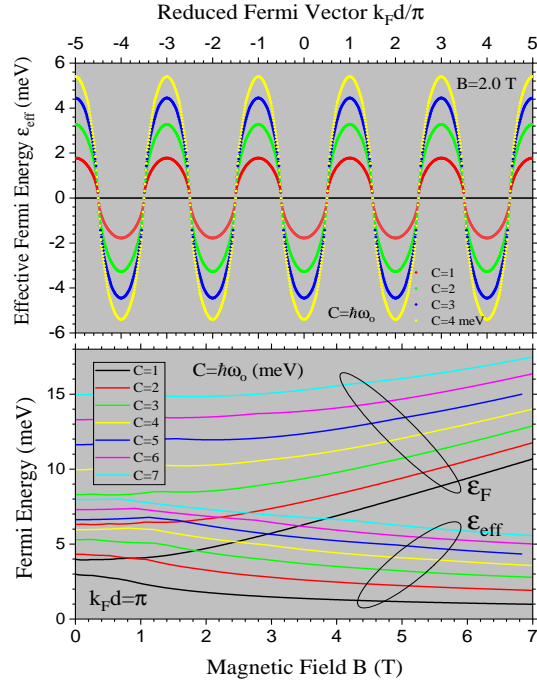


FIG. 8. (Color online) Upper panel: The effective Fermi energy vs. the reduced Fermi vector, for the magnetic field $B = 2$ T and for several values of the confinement potential. Lower panel: The Fermi energy vs. the magnetic field, for a specific value of k_F and for several values of $\hbar\omega_o$. The lower (upper) set of curves refers to the effective Fermi (Fermi) energy in the system. The band-width $W_0 = 19.76$ meV.

The upper panel of Figure 8 exemplifies the *effective* Fermi energy as a function of the reduced Fermi vector ($k_F d/\pi$) for a given value of the magnetic field B and for several values of the confinement potential $\hbar\omega_o$. The effective Fermi energy ϵ_{eff} is observed to oscillate as a function of the Fermi vector k_F for any value of $\hbar\omega_o$. Again, this oscillatory behavior is attributed to the cosine term in the single-particle energy in Eq. (7). But, in contrast to Fig. 7, the peak-to-peak amplitude of the effective Fermi energy is observed to increase with increasing confinement. This is the observation we expect intuitively for a constant – and even for zero [62] – magnetic field. The lower panel shows the Fermi energy as well as the effective Fermi energy versus the magnetic field, for a given value of the Fermi vector k_F and for several values of the confinement potential. Again, the lower set of curves representing ϵ_{eff} substantiates our observation in the upper panel. Comparing Figs. 7 and 8 leads us to infer that while the Fermi energy increases with increasing both magnetic field and confinement, the effective Fermi energy decreases (increases) with increasing magnetic field (confinement) – while keeping the confinement (magnetic field) constant.

H. The Coulombic interactions

The matrix elements of the Coulombic interactions, which inherently give the legitimacy to the formation of the collective excitations in the system, defined in Eq. (26) [or (28)] are expressed in the simplified form as follows:

$$\begin{aligned}
 U_{nn'ii'}^{mm'jj'}(q) = & \frac{2e^2}{\epsilon_b} \frac{1}{(2\pi)^2} \sqrt{\frac{n!}{(n+|m|)!}} \sqrt{\frac{n'!}{(n'+|m'|)!}} \sqrt{\frac{i!}{(i+|j|)!}} \sqrt{\frac{i'!}{(i'+|j'|)!}} \\
 & \times \int dy \int dy' e^{-y} e^{-y'} y^{|m|/2} y'^{|m'|/2} y^{|j|/2} y'^{|j'|/2} \\
 & \times L_n^{|m|}(y) L_{n'}^{|m'|}(y) L_i^{|j|}(y') L_{i'}^{|j'|}(y') \\
 & \times \int d\theta \int d\theta' e^{-i(m-m')\theta} K_o\left(q_r |y^2 + y'^2 - 2yy' \cos(\theta - \theta')|^{1/2}\right) e^{i(j-j')\theta'}. \quad (53)
 \end{aligned}$$

where $q_r = \sqrt{2}q\ell_e$ and y and y' are dimensionless variables. We have made use of the relation between the confluent hypergeometric function and the generalized Laguerre polynomial [79]

$$L_n^{(\alpha)}(y) = \binom{n+\alpha}{n} \Phi(-n, \alpha+1, y), \quad (54)$$

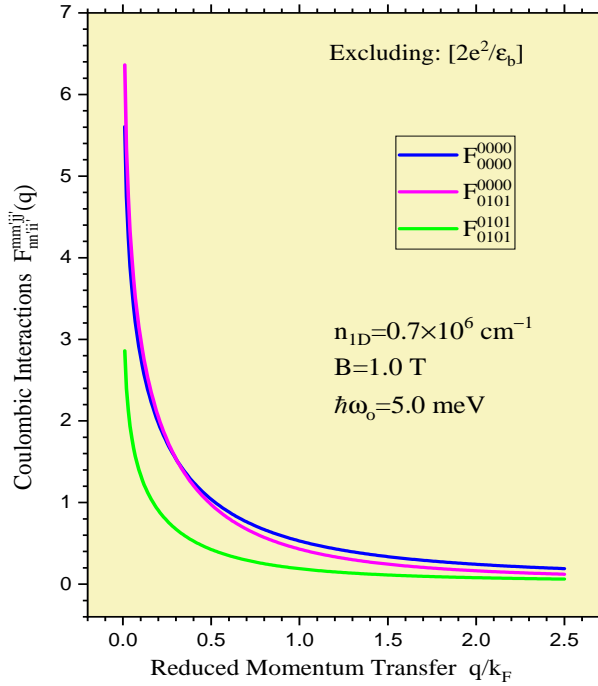


FIG. 9. (Color online) The Fourier-transformed Coulombic interactions $F_{0000}^{0000}(q)$, $F_{0101}^{0000}(q)$, and $F_{0101}^{0101}(q)$ plotted as a function of the reduced momentum transfer q/k_F . We call attention to the $F_{0101}^{0000}(q)$ being slightly dominant over the $F_{0000}^{0000}(q)$ in the range $0 \leq q/k_F \leq 0.31$ [see the text]. (After Kushwaha, Ref. 85).

Figure 9 manifests the computed matrix elements of the Fourier-transformed Coulombic interac-

tions $F_{ii'jj'}^{mm'nn'}$, where the superscripts (subscripts) refer to the orbital (principal) quantum number. The non-zerosness of these elements grants electronic excitations a many-particle character because of which the respective excitations are termed collective excitations: specifically, they are called plasmons (magnetoplasmons) depending upon whether the magnetic field is zero (nonzero) in the system. The collective excitations become Landau-damped after merging with the respective single-particle continuum in the short wavelength limit (SWL). We notice that $F_{0000}^{0000}(q) > F_{0101}^{0000}(q) > F_{0101}^{0101}(q)$ over a greater part of the momentum transfer q , except for the range of $0 < q/k_F < 0.31$ within which $F_{0101}^{0000}(q)$ is slightly greater than $F_{0000}^{0000}(q)$. Such a singular range is no trivial matter to the excitation spectrum and can (and does) have valid consequences. Concisely, within $0 < q/k_F < 0.31$, the system fosters a metastable state, which is associated with the corresponding magnetoplasmon owning a negative group velocity (NGV). The attestation of NGV signals anomalous dispersion in a gain medium with the population inversion, which is the basis for the lasing action of lasers [81, 82].

III. ILLUSTRATIVE EXAMPLES ON THE MAGNETOPLASMONS

For the illustrative numerical examples, we focus on the InAs/GaAs system just as in the original experiments [4-6]. The material parameters used are [85]: effective mass $m^* = 0.042m_0$ ($0.067m_0$) and the background dielectric constant $\epsilon_b = 13.9$ (12.8) for the InAs (GaAs). We employ the potential barrier of height $V_0 = 349.11$ meV that produces the bandwidth (of the lowest ($t = 0$) miniband) $W_0 = 19.76$ meV, in compliance with Sakaki [2] so as to minimize the optical phonon scattering. The confinement potential $\hbar\omega_0 = 5.0$ meV, the effective Fermi energy $\epsilon_{eff} = 6.4238$ meV for a 1D charge density $n_{1D} = 0.7 \times 10^6$ cm⁻¹, and the effective width of the confining (parabolic) potential well, estimated as the FWHM of the extent of the eigenfunction, $w_{eff} = 2\sqrt{2\ln(2)}\sqrt{n+1}\ell_c = 22.022$ nm. Note that the Fermi energy ϵ_F is dependent on the charge density (n_{1D}) and the confining potential ($\hbar\omega_0$). Thus, our goal is to investigate the single-particle and collective excitations in a quantum wire comprised of the VSQD in a two-subband model within the full RPA [76] at absolute zero (T=0 K). The success of RPA in such diverse geometries as the electrically/magnetically modulated systems [83] and the Rashba spintronic systems [84] is nothing but praiseworthy.

A. The influence of the layer widths

In this section, we discuss the principal results of this investigation on the excitation spectrum of the magnetized VSQD. The main aim behind discussing these results is to see the consequential changes with the variation in the well and barrier widths in the system. It has been found that the

layer widths are the most intriguing parameters and seem to drastically influence the results on the excitation spectrum. The influence of the magnetic field and/or the confinement potential on the excitation spectrum will be discussed later in a separate section.

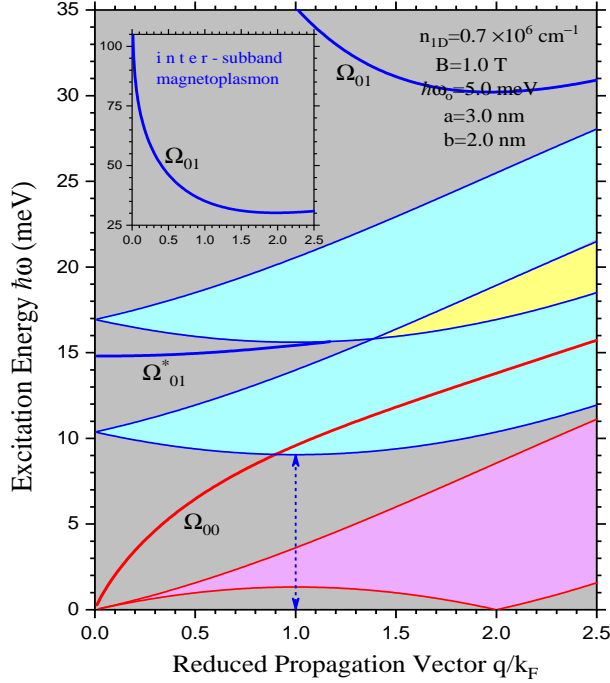


FIG. 10. (Color online) The excitation spectrum of the VSQD where the energy $\hbar\omega$ is plotted as a function of the reduced momentum transfer q/k_F in the situation where $a > b$. The shaded part in magenta (cyan) refers to the intrasubband (intersubband) SPE associated with the lowest occupied (first excited) subband at $T = 0$. The bold red (blue) curve represents the intrasubband (intersubband) CME. The vertical double-headed arrow stresses the minimum of the intersubband SPE at $q = k_F$. We call attention to gap-CME (Ω_{01}^*) which starts from the origin and propagates to merge with the lower branch of the upper split intersubband SPE before the point of intersection of the inner branches. The higher intersubband CME starts from zero with NGV, observes a minimum, and then changes the sign of its group velocity before merging with the respective SPE. All the relevant parameters are as listed inside the picture. (After Kushwaha, Ref. 85).

Figure 10 illustrates the full excitation spectrum of the resultant quantum wire comprised of the VSQD in a two-subband model within the RPA, for the case where well-width a is greater than the barrier width b . The full spectrum is composed of the single-particle excitations (SPE) and collective (magnetoplasmon) excitations (CME) for a given set of parameters: n_{1D} , $\hbar\omega_o$, B , a , and b . The figure caption specifies the SPE and CME with all essential details. The intrasubband CME (Ω_{00}) starts from the origin and propagates without tending to merge with the respective SPE up until $q/k_F = 2.5$. The intersubband SPE bifurcates at the origin and an intersubband CME (Ω_{01}^*) appears at $\hbar\omega = 14.809$ meV to propagate within the gap and finally merge with the lower edge of the upper split SPE (at $q/k_F = 1.335$, $\hbar\omega = 15.768$ meV), just before the intersection of the inner edges of the SPE. The upper intersubband CME (Ω_{01}) arises from the origin at $\hbar\omega = 102.963$ meV with a NGV

but changes its sign at $q/k_F \simeq 2.01$ to thence propagate with a positive group velocity (PGV) until it merges with the respective SPE in the SWL. The fascinating part of the excitation spectrum is that the leading CME do not merge with the respective SPE, thus do not suffer from the Landau damping, and hence remain long-lived excitations over the greater part of momentum transfer. These CME make their case effortless for the Raman scattering experiments. As to the gap-CME (Ω_{01}^*), its origination is solely ascribed to the non-zero orbital quantum number m , it is equally bonafide, and should become easily observable for all the right reasons. It is not difficult to justify the single-particle energy at the critical points: $q/k_F = 0, 1$, and 2 . The energy difference between the SPE and the CME at the origin is a manifestation of the many-body effects such as the depolarization and excitonic shifts [1]. For the set of parameters used, the mean radius of the quantum dots confined within the InAs islands is estimated (via $R_o^2/2\ell_e^2 = 1$) to be $R_o \simeq 19$ nm.

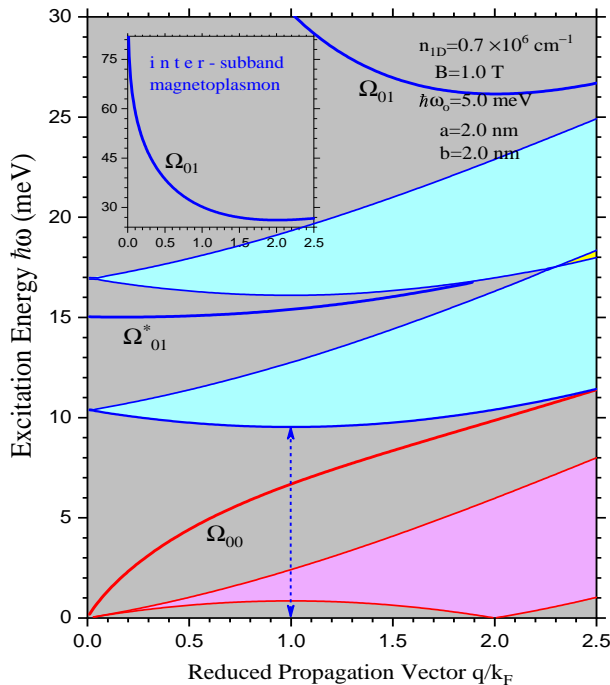


FIG. 11. (Color online) The same as in Fig. 10, but for the case where the well and the barrier widths are equal: $a = b$. The excitation spectrum observes lowering of the whole spectrum in energy and smoothing out of the big dip in the higher intersubband CME. We call attention to the point of intersection of the split intersubband SPE, which has moved to the higher momentum transfer q as compared to that in Fig. 10. Also, there is a wider gap between the intrasubband and intersubband SPE continua than seen in Fig. 10. All the relevant parameters are as listed inside the picture.

Figure 11 portrays the full excitation spectrum for the resultant system of VSQD in the situation in which well width a is equal to the barrier width b . A close comparison with Fig. 10 reveals that the whole excitation spectrum lowers in energy, the point of intersection of the inner branches of the split intersubband SPE moves towards the higher q , and a wide gap is opened up between the

intrasubband and intersubband SPEs with decreasing well-width. The intrasubband CME starts from the origin and propagates without tending to merge with the respective SPE up until $q/k_F = 2.5$. The intersubband SPE splits into two with a gap-CME (Ω_{01}^*) starting from the origin at $\hbar\omega = 15.036$ meV and propagating within the gap to merge with the lower edge of the upper split SPE at ($q/k_F = 1.893$, $\hbar\omega = 16.804$ meV), just before the point of intersection of the inner edges of the SPE. The upper intersubband CME now starts from the origin at $\hbar\omega = 82.137$ meV with the NGV but changes its sign at $q/k_F \simeq 2.01$ to propagate with PGV before it merges with the respective SPE in the short wavelength limit (SWL). As to the gap-CME (Ω_{01}^*), it remains equally bonafide, propagates up until a higher q than in Fig. 10, and should become easily observable in the Raman scattering experiments. The rest of the discussion related with Fig. 10 is still valid.

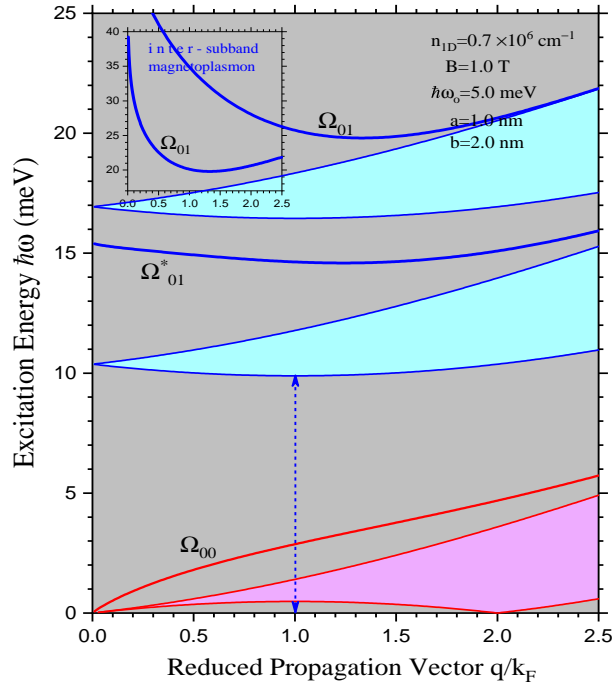


FIG. 12. (Color online) The same as in Fig. 10, but in the case where the well width is smaller than the barrier width: $a < b$. We call attention to the still further lowering of the whole spectrum in energy and a complete gap between the split intersubband SPE up until $q/k_F = 2.5$. The gap-CME has now total legitimacy and is free from the Landau damping all the way up to $q/k_F = 2.5$. There is now a larger gap between the intersubband and intrasubband SPE continua than in Fig. 11. An exact diagnosis verifies that the lower (upper) edge of the split intersubband SPE in Figs. 10 – 12 starts at 10.372 (16.936) meV.

Figure 12 shows the full excitation spectrum for the system of VSQD in the situation when the well width a is smaller than the barrier width b . A close observation reveals that the whole excitation spectrum further lowers in energy in comparison with Fig. 11, a full gap is now opened up between the split intersubband SPEs, and there is a larger gap between the intrasubband and intersubband SPEs with decreasing well-width. The intrasubband CME starts from the origin and propagates

without tending to merge with the respective SPE up until $q/k_F = 2.5$. The gap-CME (Ω_{01}^*) starts from the origin at $\hbar\omega = 15.405$ meV and propagates freely within the gap tending to merge with the upper edge of the lower split SPE somewhere in the short wavelength limit (SWL). The upper intersubband CME now starts from the origin at $\hbar\omega = 39.254$ meV with the NGV but changes its sign at $q/k_F \simeq 1.33$ to propagate with positive group velocity in the close vicinity of $-$ but without merging with $-$ the upper edge of the upper split intersubband SPE up until $q/k_F = 2.5$. The rest of the discussion related with Fig. 10 is still valid.

B. The influence of the magnetic field

The complete excitation spectrum of a system – within a specified model – is comprised of the single-particle and the collective excitations plotted together. Interestingly, the role of the single-particle excitations in the full spectrum is two-fold: (i) to define the propagation range of the collective excitations, and (ii) to specify whether or not they are free from Landau damping within the given $\omega-q$ space. In other words, the single-particle excitations specify the life of and provide the legitimacy to the collective excitations. However, it is up to the bonafide collective excitations to profess their role in the device design – for a given set of parameters.

Figure 13 displays the energy of the collective (magnetoplasmon) excitations versus the reduced momentum transfer for a given confinement potential and for several values of the applied magnetic field. We choose the set of parameters corresponding to that for Fig. 12. This implies three clear-cut CMEs: the intrasubband CME (Ω_{00}), the gap-CME (Ω_{01}^*), and the highest CME (Ω_{01}) which emerges from the origin with a NGV plotted, respectively, in the lower, the middle, and the upper panels. As stated above, we have avoided to plot the respective single-particle excitations in order not to make a mess in the picture. What we observe in this figure is obviously what we intuitively expect: the energy of the magnetoplasmon excitations increases with increasing magnetic field. It is worth mentioning that this observation remains true independently of the size, shape, and dimensions of the system – with a very few exceptions. It is interesting to note that while Ω_{00} indicates a monotonous increase in the energy, Ω_{01}^* shows a tendency to emerge with an NGV, and Ω_{01} generally maintains the trend of originating with an NGV – with increasing magnetic field. The gap-CME and the uppermost CME, which start with an NGV, generally, observe a minimum before changing the sign of their group velocity and thence propagate with a PGV until they merge with the respective SPE and become Landau-damped at the higher momentum transfer.

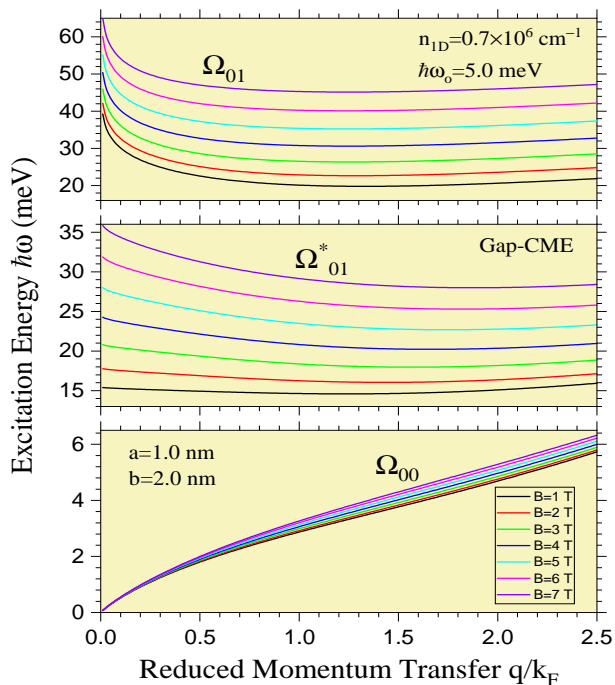


FIG. 13. (Color online) The collective (magnetoplasmon) excitation spectrum within a two-subband model where the energy $\hbar\omega$ is plotted as a function of the reduced momentum transfer q/k_F , for several values of the magnetic field B . The other parameters are as listed inside the picture. Notice that we have only plotted the bonafide intrasubband and intersubband collective (magnetoplasmon) excitations, which remain Landau-undamped until a very large momentum transfer.

C. On the inverse dielectric functions

The diehard, traditional, condensed-matter theorists recognize that searching the zeros of the dielectric function and the poles of the inverse dielectric function (IDF) must, in principle, produce identical results for the excitation spectra in a system [78]. This is very true but not without certain reservations. The latter has for sure characteristic advantages over the former. For instance, the imaginary (real) part of the IDF furnishes a significant measure of the longitudinal (Hall) resistance in the system. This indicates that investigating IDF allows us to comprehend not only the optical but also the transport phenomena in a system of interest. Besides, examining $\text{Im} [\epsilon^{-1}(q, \omega)]$ also tacitly provides precise details of the inelastic electron (or Raman) scattering cross-section in the system. In relation to the inelastic electron scattering, $\text{Im} [\epsilon^{-1}(q, \omega)]$ plays a central role in studying such remarkable phenomena as the fast-particle energy loss to the nanostructure in question.

Figure 14 depicts the inverse dielectric function versus the excitation energy of the system, for various values of the momentum transfer q/k_F . The real (imaginary) parts of the IDF are plotted as solid (dashed) curves for a given q/k_F . Since we have handpicked relatively small values of q/k_F , we must anticipate reproducing the collective (rather than the single-particle) excitations. It is verified

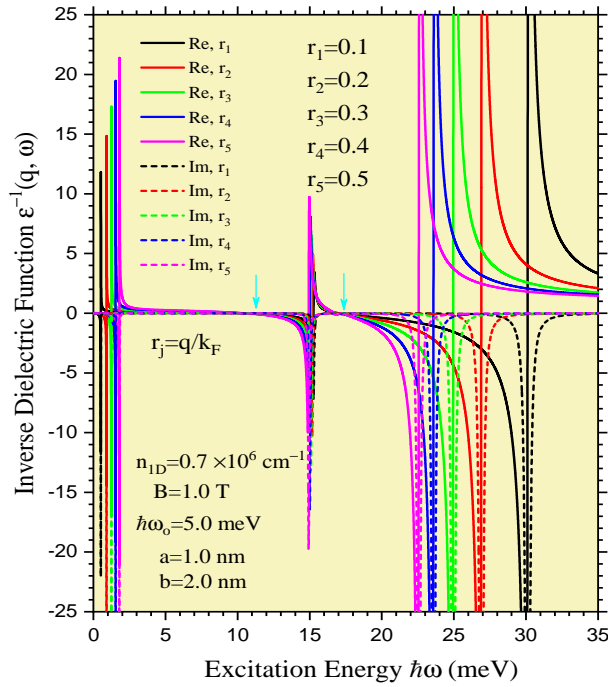


FIG. 14. (Color online) Inverse dielectric function $\epsilon^{-1}(q, \omega)$ vs. the excitation energy $\hbar\omega$ for the given values of the momentum transfer q/k_F . The other parameters are listed in the picture. (After Kushwaha, Ref. 85).

that all three peaks, for a given q/k_F , correspond to the respective CME in the excitation spectrum. A small energy span covered by the middle peaks – pertaining to the gap-CME (Ω_{01}^*) – indicates that the gap-mode is pretty much flat in the long wavelength limit (LWL), which is very true (see, e.g., Figs. 10-12). To be specific, the resonance peaks arising at $\hbar\omega$ (meV) = 0.519, 0.913, 1.247, 1.542, and 1.807, for example, reproduce the intrasubband CME in Fig. 12. The resonance peaks occurring at $\hbar\omega$ (meV) = 15.312, 15.217, 15.131, 14.961, and 14.885 yield the gap-CME in Fig. 12. With the same token, the peaks at $\hbar\omega$ (meV) = 30.018, 26.816, 24.876, 23.513, and 22.631 furnish the upper intersubband CME in Fig. 12. It is noteworthy that both the gap-CME and the upper CME are seen to exist in the reverse order to the values of q . This is because both the gap-CME and the upper CME propagate with a NGV until they observe a minimum. The details of the magnetorotonic character of the upper CME are deferred to a future publication.

Figure 15 instances the inverse dielectric function versus the momentum transfer of the system q/k_F , for several values of the excitation energy $\hbar\omega$. The real (imaginary) parts of the IDF are plotted as solid (dashed) curves for a given value of $\hbar\omega$. Needless to say the quantity that directly strikes the quantum transport is the spectral weight $\text{Im}[\epsilon^{-1}(q, \omega)]$ which controls both the single-particle contribution at large momentum transfer (q) and the collective (magnetoplasmon) contribution at small q . Given the set of the selected excitation energies $\hbar\omega = 1.0, 2.0, 15.0,$ and 20.0 , we expect to have covered parts of all three CME as well as the intrasubband SPE in Fig. 12. The pair of red and

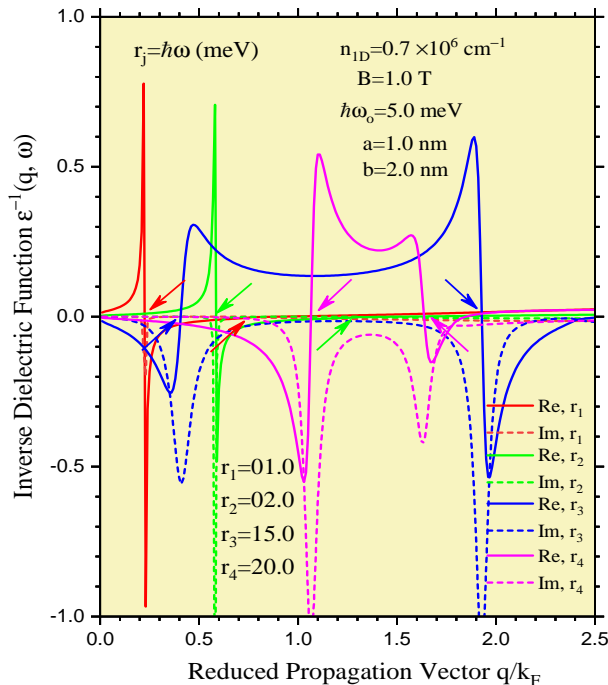


FIG. 15. (Color online) Inverse dielectric function $\epsilon^{-1}(q, \omega)$ vs. the momentum transfer q/k_F for the given values of the excitation energy $\hbar\omega$. The other parameters are as listed inside the picture. A pair of identical colored arrows indicate the resonance peaks and the *crossings* of the real and imaginary parts, which we assume must yield a good correspondence with Fig. 12.

green arrows indicating the resonance peaks at $(q/k_F = 0.226, \hbar\omega = 1.0)$ and $(q/k_F = 0.582, \hbar\omega = 2.0)$ the crossings at $(q/k_F = 0.763, \hbar\omega = 1.0)$ and $(q/k_F = 1.305, \hbar\omega = 2.0)$ reproduce, respectively, the intrasubband CME (Ω_{00}) and the SPE in Fig. 12. The pair of blue arrows indicating the resonance peaks at $(q/k_F = 0.405, \hbar\omega = 15.0)$ and $(q/k_F = 1.925, \hbar\omega = 15.0)$ reproduce the gap-CME (Ω_{01}^*) in Fig. 12. Similarly, the pair of magenta arrows indicating the resonance peaks at $(q/k_F = 1.065, \hbar\omega = 20.0)$ and $(q/k_F = 1.636, \hbar\omega = 20.0)$ reproduce the uppermost intersubband CME (Ω_{01}) in Fig. 12. As such, Figs. 14 and 15 substantiate the fact that the zeros of the DF and the poles of the IDF yield exactly identical results (see above). However, this is merely a glimpse of the efficacy of the IDF. In order to commend fully the role of IDF, one has to dive deep down to learn their exact analytical diagnosis as well as to pursue their practicality for a given system [78].

IV. CONCLUDING REMARKS

In summary, the author has investigated the single-particle and collective (magnetoplasmon) excitations in a resultant system of quantum wire made up of the VSQD subjected to a 2D (planar) confining (parabolic) potential and an applied magnetic field in the symmetric gauge within a two-subband model in the framework of full RPA. The noteworthy features of this report are the following:

(i) the B-dependence of the DOS authenticating the claim of VSQD mimicking a realistic quantum wire, (ii) the Fermi energy oscillating as a function of the Bloch vector, (iii) an unusual bifurcating of the intersubband SPE at the origin owing to the non-zero B, (iv) the existence of a bonafide CME within the gap of the split SPE, (v) all three CME – including the gap mode – being free from the Landau damping up until a relatively large momentum transfer, (vi) the gap CME becoming better defined and remaining Landau-undamped even in the SWL ($q/k_F \geq 2$) with decreasing period of the system, (vii) The creation of very very high-energy (upper) intersubband CME in the LWL, (viii) the upper intersubband CME propagating largely with the NGV until a wave vector twice the Fermi vector, (ix) the B-dependence of the IDF setting to furnish a significant measure of the transport phenomena in the system. We have neglected the strain effect because its influence on the collective excitations – plasmons and/or magnetoplasmons – is practically nonexistent. Finally, the exact IDF as studied here knows no bounds regarding the subband occupancy and serves a useful purpose of analyzing the inelastic electron (and Raman) scattering experiments. In a nutshell, the small length scales and the strong coupling along the growth axis effectuate the resultant nanostructure of VSQD to mimic a realistic quantum wire. This clearly emboldens our confidence in the theoretical framework of the problem and brings our quest for *reversing the trend* to a fruitful finish. The size-dependence of the tunability of the energy range achieved by the CME makes the periodic system of VSQD a prospective source of offering magnetoplasmon qubits with a super high-speed advantage over the exciton qubits – particularly in the LWL [86]. Given the realistic set of geometric and material parameters – which are within the reach of the current nanotechnology – involved in the process, the realization of the periodic system of VSQD seems to be a fact rather than a fiction. We believe that such behavior characteristics of the CME as investigated and predicted here can be successfully observed by the resonant Raman scattering experiments. Consequently, the magnetized chain of VSQD must serve to be a potentially viable system for implementing the formal idea of quantum state transfer for the quantum computation and the quantum communication networks.

ACKNOWLEDGMENTS

This work is a comprehensive version of a *Letter* recently published in EPL (see Ref. 85). The author has benefited from stimulating discussions and communications with some outstanding colleagues in the field. I would like to particularly thank Hiroyuki Sakaki, Allan MacDonald, Bahram Djafari-Rouhani, Peter Nordlander, and Douglas Natelson to mention a few. I also wish to acknowledge Kevin Singh for the timely assistance with the software during the course of this work.

Data Availability: The data that support the findings of this study are available within the article.

- [1] For an extensive review of electronic, optical, and transport phenomena in the systems of reduced dimensions, such as quantum wells, quantum wires, quantum dots, and (electrically/magnetically) modulated systems, see M.S. Kushwaha, Surf. Sci. Rep. **41**, 1 (2001).
- [2] H. Sakaki, Jpn. J. Appl. Phys. **28**, L314 (1989).
- [3] B.Y.K. Hu and S. Das Sarma, Phys. Rev. Lett. **68**, 1750 (1992).
- [4] Q. Xie, A. Madhukar, P. Chen, and N.P. Kobayashi, Phys. Rev. Lett. **75**, 2542 (1995).
- [5] G.S. Solomon, J.A. Trezza, A.F. Marshall, and J.S. Harris, Phys. Rev. Lett. **76**, 952 (1996).
- [6] M.S. Miller, Jpn. J. Appl. Phys. **36**, 4123 (1997).
- [7] T. Inoue, M. Asada, N. Yasuoka, T. Kita, and O. Wada, J. Phys.: Conf. Series **245**, 012076 (2010).
- [8] Y. Shoji, R. Oshima, A. Takata, and Y. Okada, J. Cryst. Growth **312**, 226 (2010).
- [9] Ch. Huang, M. Igarashi, S. Horita, M. Takeguchi, Y. Uraoka, T. Fuyuki, I. Yamashita, and S. Samukawa, Jap. J. App. Phys. **49**, 04DL16 (2010).
- [10] S.K. Zhang, Th. Myint, W.B. Wang, B.B. Das, N. Perez-Paz, H. Lu, M.C. Tamargo, A. Shen, and R. R. Alfano, J. Vac. Sci. Technol. B **28**, C3D17 (2010).
- [11] J.J. Zhang, N. Hrauda, H. Groiss, A. Rastelli, J. Stangl, F. Schäffler, O.G. Schmidt, and G. Bauer, Appl. Phys. Lett. **96**, 193101 (2010).
- [12] T. Inoue, M. Asada, N. Yasuoka, O. Kojima, T. Kita, O. Wada, Appl. Phys. Lett. **96**, 211906 (2010).
- [13] Y. Shoji, R. Oshima, A. Takata, and Y. Okada, Physica E **42**, 2768 (2010).
- [14] G. Koblmuller, S. Hertenberger, K. Vizbaras, M. Bichler, F. Bao, J.P. Zhang, and G. Abstreiter, Nanotechnology **21**, 365602 (2010).
- [15] O. Moshe, D.H. Rich, B. Damilano, and J. Massies, J. Phys. D: Appl. Phys. **44**, 505101 (2011).
- [16] K. Kuklinski, L. Kłopotowski, K. Fronc, P. Wojnar, T. Wojciechowski, M. Czapkiewicz, J. Kossut, G. Karczewski and T. Wojtowicz, Acta Physica Polonica A **120**, 856 (2011).
- [17] Y. Ikeuchi, T. Inoue, M. Asada, Y. Harada, T. Kita, E. Taguchi, and H. Yasuda. Appl. Phys. Express **4** 062001 (2011).
- [18] W.S. Liu, H.M. Wu, Y.A. Liao, J.I. Chyi, W.Y. Chen, and T.M. Hsu, J. Cryst. Growth **323**, 164 (2011).
- [19] K.N. Hui and K.S. Hui, Current Appl. Phys. **11**, 662 (2011).
- [20] S.S. Walavalkar, A.P. Homyk, C.E. Hofmann, M.D. Henry, C. Shin, H.A. Atwater, and A. Scherer,

- Appl. Phys. Lett. **98**, 153114 (2011).
- [21] K. Akahane, N. Yamamoto, M. Naruse, T. Kawazoe, T. Yatsui, and M. Ohtsu, *Jap. J. Appl. Phys.* **50**, 04DH05 (2011).
- [22] D. Kim, S.G. Carter, A. Greulich, A.S. Bracker and D. Gammon, *Nature Phys.* **7**, 223 (2011).
- [23] T.W. Saucer, J.E. Lee, A.J. Martin, D. Tien, J.M. Millunchick, and V. Sih, *Solid State Commun.* **151**, 269 (2011).
- [24] K. Muller, A. Bechtold, C. Ruppert, C. Hautmann, J. S. Wildmann, T. Kaldewey, M. Bichler, H. J. Krenner, G. Abstreiter, M. Betz, and J. J. Finley, *Phys. Rev. B* **85**, 241306 (2012).
- [25] D. Hauser, G. Savelli, M. Plissonnier, L. Montès, and J. Simon, *Thin Solid Films* **520**, 4259 (2012).
- [26] E. Koroknay, W.M. Schulz, D. Richter, U. Rengstl, M. Reischle, M. Bommer, Ch. A. Kessler¹, Robert Roßbach, H. Schweizer, M. Jetter, and P. Michler, *Phys. Stat. Solidi B* **249**, 737 (2012).
- [27] B. Diaz, A. Malachias, L.A. Montoro, P.H.O. Rappl, E. Abramof, *Nanotechnology* **23**, 015604 (2012).
- [28] I.H. Chen, K.H. Chen, C.C. Wang, and P.W. Li, *ECS Transactions* **50**, 313 (2012).
- [29] A. Greulich, S.C. Badescu, D. Kim, A.S. Bracker, and D. Gammon, *Phys. Rev. Lett.* **110**, 117402 (2013).
- [30] T. Sugaya, R. Oshima, K. Matsubara, and S. Niki, *J. Appl. Phys.* **114**, 014303 (2013).
- [31] A. Takahashi, T. Ueda, Y. Bessho, Y. Harada, and T. Kita, *Phys. Rev. B* **87**, 235323 (2013).
- [32] K.G. Eyink, L.J. Bissell, J. Shoaf, D.H. Tomich, D. Esposito, M. Hill, L. Grazulis, A. Aronow, and K. Mahalingam, *J. Vac. Sci. Technol.* **31**, 03C131 (2013).
- [33] D.Y. Oh, S.H. Kim, J. Huang, A. Scofield, D. Huffaker, A. Scherer, *Nanotechnology* **24**, 265201 (2013).
- [34] Y. Shoji, K. Akimoto and Y. Okada, *J. Phys. D: Appl. Phys.* **46**, 024002 (2013).
- [35] M. Suwa, A. Takahashi, T. Ueda, B. Yusuke, Y. Harada, T. Kita, *Phys. Stat. Solidi C* **10**, 1492 (2013).
- [36] A.I. Yakimov, V.V. Kirienko, V.A. Armbrister, A.A. Bloshkin, and A.V. Dvurechenskii, *Phys. Rev. B* **90**, 035430 (2014).
- [37] D. Sonnenberg, A. Küster, A. Graf, Ch. Heyn and W. Hansen, *Nanotechnology* **25**, 215602 (2014).
- [38] J. Wu, Y. Hirono, X. Li, Z.M. Wang, J. Lee, M. Benamara, S. Luo, Y.I. Mazur, E.S. Kim, and G.J. Salamo, *Adv. Funct. Mater.* **24**, 530 (2014).
- [39] V. Tasco, M. Usman, M.D. Giorgi and A. Passaseo, *Nanotechnology* **25**, 055207 (2014).
- [40] V. Lopes-Oliveira, Y.I. Mazur, L.D. de Souza, L.A.B. Marcal, J. Wu, M.D. Teodoro, A. Malachias, V.G. Dorogan, M. Benamara, G.G. Tarasov, E. Marega, G.E. Marques, Zh. M. Wang, M. Orlita, G.J. Salamo, and V. Lopez-Richard, *Phys. Rev. B* **90**, 125315 (2014).
- [41] Yu.I. Mazur, V. Lopes-Oliveira, L.D. de Souza, V. Lopez-Richard, M.D. Teodoro, V.G. Dorogan, M. Benamara, J. Wu, G.G. Tarasov, E. Marega, Z. M. Wang, G.E. Marques, and G.J. Salamo, *J. Appl.*

- Phys. **117**, 154307 (2015).
- [42] J.H. Park, A. Mandal, D.Y. Um, S. Kang, D. Lee, and C.R. Lee, RSC Advances **5**, 47090 (2015).
- [43] C.M. Chow, A.M. Ross, D. Kim, D. Gammon, A.S. Bracker, L.J. Sham, and D.G. Steel, Phys. Rev. Lett. **117**, 077403 (2016).
- [44] M.H. Kuo, S.K. Chou, Y.W. Pan, S.D. Lin, T. George, and P.W. Li, J. Appl. Phys. **120**, 233106 (2016).
- [45] Y.H. Roh, S.J. Sim, I.J. Cho, N. Choi, and K.W. Bong, Analyst **141**, 4578 (2016).
- [46] A. Küster, Ch. Heyn, A. Ungeheuer, G. Juska, S.T. Moroni², E. Pelucchi and W. Hansen, Nanoscale Res. Lett. **11**, 282 (2016).
- [47] W. Xu, W. Liu, J.F. Schmidt, W. Zhao, X. Lu, T. Raab, C. Diederichs, W. Gao, D.V. Seletskiy and Q. Xiong, Nature **541**, 62 (Jan 5, 2017).
- [48] Y. Zhang, K.G. Eyink, L. Grazulis, M. Hill, J. Peoples, K. Mahaling, J. Cryst. Growth **477**, 19 (2017).
- [49] D.H. Yeon, B.C. Mohanty, C.Y. Lee, S.M. Lee, and Y.S. Cho, ACS Omega **2**, 4894 (2017).
- [50] X. Tang, F. Wu, and King W.Ch. Lai, Appl. Phys. Lett. **110**, 241104 (2017).
- [51] X. Song, Y. Zhang, H. Zhang, Y. Yu, M. Cao, Y. Che, H. Dai, J. Yang, X. Ding, and J. Yao, Nanotechnology **28**, 145201 (2017).
- [52] R. Long, D. Casanova, W.H. Fang, and O.V. Prezhdo, J. Am. Chem. Soc. **139**, 2619 (2017).
- [53] A. Mohanta, D.J. Jang, S.K. Lu, D.Ch. Ling, and J.S. Wang, Appl. Phys. Lett. **110**, 033107 (2017).
- [54] I. Seker, A. Karatutlu, O. Gurbuz, S. Yanik, Y. Bakis, and M. Karakiz, Appl. Phys. A **124**, 47 (2018)
- [55] S. Blumenthal, T. Rieger, D. Meertens, A. Pawlis, D. Reuter, and D.J. As, Phys. Stat. Solidi B **255**, 1600729 (2018).
- [56] A. Lin, M.F. Doty, and G.W. Bryant, Phys. Rev. B **99**, 075308 (2019).
- [57] H.Y. Ramirez and Shun-Jen Cheng, Phys. Rev. Lett. **104**, 206402 (2010).
- [58] A.I. Yakimov, A.A. Bloshkin, and A.V. Dvurechenskii, Phys. Rev. B **81**, 115434 (2010).
- [59] K. Gawarecki, M. Pochwała, A. Grodecka–Grad, and P. Machnikowski, Phys. Rev. B **81**, 245312 (2010).
- [60] I. Mondragon-Shem, B.A. Rodríguez, and F.E. López, Comput. Phys. Commun. **181**, 1510 (2010).
- [61] S. Prabhakar and R. Melnik, J. Appl. Phys. **108**, 064330 (2010).
- [62] M.S. Kushwaha, J. Chem. Phys. **135**, 124704 (2011); and references therein.
- [63] K. Gawarecki and P. Machnikowski, Acta. Phys. Pol. **119**, 637 (2011).
- [64] A. Sitek and P. Machnikowski, Phys. Rev. B **86**, 205315 (2012).
- [65] M. Usman, Phys. Rev. B. **86**, 155444 (2012).
- [66] Li-Bo Chen, L.J. Sham, E. Waks, Phys. Rev. B. **85**, 115319 (2012).
- [67] W.J. Pasek, M.P. Nowak, and B. Szafran, Phys. Rev. B. **89**, 245303 (2014).

- [68] Li-Bo Chen and W. Yang, *Laser Phys. Lett.* **11**, 105201 (2014).
- [69] K. Gawarecki, P. Machnikowski, and T. Kuhn, *Phys. Rev. B.* **90**, 085437 (2014).
- [70] P. Karwat, and P. Machnikowski, *Phys. Rev. B.* **91**, 125428 (2015).
- [71] T. Kawazu, *Jap. J. Appl. Phys.* **54**, 04DJ01 (2015).
- [72] C. Segarra, J.I. Climente, F. Rajadell, and J. Planelles, *J. Phys.: Condens. Matter* **27**, 415301 (2015).
- [73] X. Ma, G.W. Bryant, and M.F. Doty, *Phys. Rev. B.* **93**, 245402 (2016).
- [74] J.R. Jarzynka, P.G. MacDonald, J. Shumway, and I. Galbraith, *J. Appl. Phys.* **119**, 224303 (2016).
- [75] P. Karwat, K. Gawarecki, and P. Machnikowski, *Phys. Rev. B.* **95**, 235421 (2017).
- [76] B. Ilahi, K. Alshehria, N.A. Madhar, L. Sfaxi, H. Maaref, *Results in Phys.* **9**, 904 (2018).
- [77] D. Pines, *The Many-Body Problem* (Benjamin, New York, 1961); A.L. Fetter and J.D. Walecka, *Quantum Theory of Many-Particle Systems* (McGraw-Hill, New York, 1971); G.D. Mahan, *Many Particle Physics* (Plenum, New York, 1981).
- [78] M.S. Kushwaha, *AIP Advances* **2**, 032104 (2012); **3**, 042103 (2013); **6**, 035014 (2016); **4**, 127151 (2014). These offer the exact derivations of the inverse dielectric functions (IDF) for the Q-2D, Q-1D, and Q-0D electron systems of current interest and their ability to interpret the two catholic experiments – inelastic electron scattering and inelastic light (or Raman) scattering – in condensed matter physics.
- [79] M. Abramowitz and I. A. Stegun, *Handbook of Mathematical Functions* (Dover, New York, 1972); J. Spanier and K. B. Oldham, *An Atlas of Functions* (Springer-Verlag, Berlin, 1987); I.S. Gradshteyn and I.M. Ryzhik, *Tables of Integrals, Series, and Products* (Academic, New York, 1994).
- [80] G. Bastard, *Phys. Rev. B* **24**, 5693 (1981). The so-called “Bastard’s boundary conditions” were known in the literature much before Bastard used them. See, e.g., D.J. BenDaniel and C.B. Duke, *Phys. Rev.* **152**, 683 (1966).
- [81] M.S. Kushwaha, *Phys. Rev. B* **78**, 153306 (2008); *J. Appl. Phys.* **109**, 106102 (2011); *Mod. Phys. Lett. B* **28**, 1430013 (2014).
- [82] M.S. Kushwaha, *Europhys. Lett.* **123**, 34001 (2018); *Mod. Phys. Lett. B* **33**, 1950062 (2019); This contains an Appendix on the gauge invariance.
- [83] M.S. Kushwaha and H. Sakaki, *Phys. Rev. B* **69**, 155331 (2004); *Solid State Commun.* **130**, 717 (2004).
- [84] M.S. Kushwaha, *Phys. Rev. B* **74**, 045304 (2006); **76**, 245315 (2007); *J. Appl. Phys.* **104**, 083714 (2008).
- [85] M.S. Kushwaha, *Europhys. Lett.* **127** 37004 (2019).
- [86] The precise diagnosis of the thematic observations such as the negative group velocity, the magnetorotonic character, and the greater-speed magnetoplasmon qubits associated with the highest magnetoplasmons (in Figs. 10-12) is beyond the scope of this work and hence deferred to a future publication.